


# Tracing the magnetic field morphology of the LDN 1172/1174 cloud complex

Piyali Saha<sup>1,2,3</sup> , Maheswar Gopinathan<sup>1</sup>, Ekta Sharma<sup>1,4</sup>, Chang Won Lee<sup>5,6</sup>, Tuhin Ghosh<sup>7</sup>, and Shinyoung Kim<sup>5</sup>

<sup>1</sup> Indian Institute of Astrophysics (IIA), Sarjapur Road, Koramangala, Bangalore 560034, India  
e-mail: s.piyali16@gmail.com

<sup>2</sup> Satyendra Nath Bose National Centre for Basic Sciences (SNBNCBS), Salt Lake, Kolkata-700 106, India

<sup>3</sup> Pt. Ravishankar Shukla University, Amanaka G.E. Road, Raipur, Chhatisgarh 492010, India

<sup>4</sup> Department of Physics and Astrophysics, University of Delhi, Delhi 110007, India

<sup>5</sup> Korea Astronomy, and Space Science Institute (KASI), 776 Daedeokdae-ro, Yuseong-gu, Daejeon 305-348, Republic of Korea

<sup>6</sup> University of Science and Technology, Korea, 217 Gajeong-ro, Yuseong-gu, Daejeon 34113, Republic of Korea

<sup>7</sup> School of Physical Sciences, National Institute of Science Education and Research, HBNI, Jatni 752050, Odisha, India

Received 20 November 2020 / Accepted 7 June 2021

## ABSTRACT

**Context.** The LDN 1172/1174 cloud complex in the Cepheus Flare region presents a hub-filament structure with the reflection nebula, NGC 7023, illuminated by a Herbig Be star, HD 200775, which consists of the hub with a  $\sim 5$  pc long narrow filament attached to it. Formation of a sparse cluster of low- and intermediate-mass stars is presently taking place in the hub.

**Aims.** The aim of this work is to map the magnetic field geometry of LDN 1172/1174 to understand the role played by the field lines in the formation of the molecular cloud.

**Methods.** Unpolarized background stars can be used to measure dichroically polarized light produced by the magnetically aligned grains present in molecular clouds. As these dust grains get aligned with their minor axes parallel to the ambient magnetic field, the polarization measurements can provide the plane-of-sky component of the magnetic field. We made *R*-band polarization measurements of 249 stars projected on the entire LDN 1172/1174 cloud complex to map the geometry of the magnetic field of this region.

**Results.** The magnetic field geometry constructed from our *R*-band polarization measurements is found to be parallel to the elongated structure inferred from the column density distribution of the cloud produced using the *Herschel* images. Our *R*-band polarization measurements are found to be in good agreement with those obtained from *Planck*. There is evidence of a possible distortion of the magnetic fields toward the northwestern part of the cloud by HD 200775. The magnetic field strength is estimated as  $\sim 30$   $\mu$ G. The estimated star formation rate (SFR)/mass of  $2.0 \pm 1.3\%$   $\text{Myr}^{-1}$  and  $0.4 \pm 0.3\%$   $\text{Myr}^{-1}$  for LDN 1172/1174 and the neighboring cloud complex, LDN 1147/1158, respectively, are found to be consistent with the mean SFR/mass found for the clouds with magnetic field orientations parallel and perpendicular to their elongated structures, respectively. These results support earlier findings that the clouds with magnetic field lines parallel to their long axes seem to have higher SFRs compared to those with the magnetic field orientation perpendicular to the cloud elongation.

**Key words.** techniques: polarimetric – stars: formation – ISM: clouds – ISM: magnetic fields

## 1. Introduction

Star formation is often found to be associated with the densest regions of molecular clouds that are elongated and filamentary in shape. In fact, results obtained with the *Herschel* space observatory (Pilbratt et al. 2010) of nearby interstellar clouds, as well as in more distant and massive clouds, reveal the ubiquity of complex networks of filaments (André et al. 2010; Molinari et al. 2010; Hill et al. 2011). How molecular clouds form and then evolve into filaments and cores and finally collapse to form stars is still a puzzle. Turbulence, gravity, and magnetic fields are believed to collaborate or compete in the process of the formation of these observed structures (e.g., Klessen et al. 2000; Ballesteros-Paredes et al. 2007; André et al. 2010; Molina et al. 2012; Kirk et al. 2015; Beattie & Federrath 2020). However, the relative importance of these three factors in the whole process remains to be unraveled.

Several observations have presented evidence for a longitudinal flow of material along the filaments, leading to the idea that the filaments are long-lived but out-of-equilibrium flow

structures that supply material to the central high-density hubs, the locations where the filaments converge to form an intricate and inhomogeneous network of filaments that in turn appear to accrete material from their surroundings (Schneider et al. 2010; Kirk et al. 2013; Gómez & Vázquez-Semadeni 2014; Jiménez-Serra et al. 2014; Peretto et al. 2014; Hajigholi et al. 2016; Rayner et al. 2017; Gómez et al. 2018; Dutta et al. 2018; Lu et al. 2018; Williams et al. 2018; Chen et al. 2019; Shimajiri et al. 2019; Treviño-Morales et al. 2019). Because these filaments are denser than their ambient medium, it is believed that some compression is essentially involved in their formation mechanism (Hennebelle 2013). This led to the suggestion that filamentary structures are formed by gravitational and/or turbulent compressive motions (e.g., Padoan et al. 2001; Hartmann et al. 2001; Padoan & Nordlund 2002; Ballesteros-Paredes et al. 2007; Arzoumanian et al. 2011). The magnetic fields are expected to play a vital role by acting as agents that help to channel cloud accumulation and fragmentation (e.g., Nagai et al. 1998; Fiege & Pudritz 2000; Shetty & Ostriker 2006; Van Loo et al. 2014; Seifried & Walch 2015). Results from a study conducted by

Gómez et al. (2018) to investigate the structure of the magnetic field inside a self-gravitating filament formed in a turbulent environment suggest that the magnetic field geometry represents the flow pattern of the material inside and in the vicinity of the filaments. As cloud material tends to flow along the magnetic field lines, forming sheets or filaments, the low-density striations or low-column-density material tends to align parallel to the magnetic fields (Palmeirim et al. 2013; André & Kremer 2014; Zamora-Avilés et al. 2017). The gas around the filaments gets accreted onto them, making the field lines become oriented perpendicular to the filaments, which is often found in observations and simulations (Goodman et al. 1992; Chapman et al. 2011; Sugitani et al. 2011; Gómez & Vázquez-Semadeni 2014; Gómez et al. 2018). But as the gas density increases, the flow pattern changes as an effect of the gravity-driven motion of cloud material. The longitudinal flow of material toward the clumps drags the field lines along with it, making the field lines parallel to the filaments (Pillai et al. 2020). Results from several studies have shown that the velocity and the magnetic fields are preferentially aligned (Matthaeus et al. 2008; Banerjee et al. 2009; Iffrig & Hennebelle 2017). These results are consistent with the correlations found between the magnetic field direction and the density gradient (Soler et al. 2013; Koch et al. 2013, 2014; Planck Collaboration Int. XXXV 2016; Soler & Hennebelle 2017). When magnetic field lines from opposite sides of the filament are connected, the resulting field lines become perpendicular at the internal vicinity of the filament (Gómez et al. 2018).

Polarization observations in optical (e.g., Vrba et al. 1976; Goodman et al. 1990; Bhatt & Jain 1992; Alves et al. 2008; Franco et al. 2010; Neha et al. 2016, 2018), near-infrared (e.g., Sato et al. 1988; Goodman et al. 1995; Sugitani et al. 2010; Tamura et al. 2011; Soam et al. 2015a; Eswaraiah et al. 2017), and submillimeter wavelengths (e.g., Matthews et al. 2009; Ward-Thompson et al. 2000; Qiu et al. 2014; Planck Collaboration Int. XXXV 2016; Soam et al. 2018b) have revealed the ubiquity of magnetic fields in the Galaxy. Studies that probed the relative orientation between the magnetic field and the elongated cloud structure suggest that they tend to be oriented either parallel or perpendicular to each other (Goodman et al. 1990, 1992; Chapman et al. 2011; Li et al. 2014; Sugitani et al. 2011). The low-column-density structures are preferably oriented parallel to the local mean magnetic field, and the high-column-density structures are statistically oriented perpendicular to the same (Li et al. 2011, 2013; Palmeirim et al. 2013; Heyer et al. 2016; Planck Collaboration Int. XXXV 2016; Alina et al. 2019). These findings are also consistent with the results obtained from numerical simulations (e.g., Stone et al. 1998; Nagai et al. 1998; Nakamura & Li 2008; Hennebelle 2013; Van Loo et al. 2014; Chen & Ostriker 2014; Inutsuka et al. 2015; Wareing et al. 2016; Tritsis & Tassis 2016). While the polarization measurements in optical wavelengths can trace the field geometry in low-density inter-cloud media (ICM) and the periphery of molecular clouds, the polarized thermal emission due to the dust can trace the fields in the high-density parts of the cloud (e.g., Ward-Thompson et al. 2009; Li et al. 2009; Soam et al. 2019; Sharma et al. 2020). Thus, by comparing the magnetic field geometry inferred from the optical and submillimeter wavelengths, the relationship between the magnetic field orientations inside the cloud and the ICM can be investigated.

The LDN 1172/1173/1174 (hereafter L1172/1174; Lynds 1962) cloud complex was shown by Myers (2009) to be one of the typical examples of a hub-filament structure. The reflection nebula, NGC 7023, is illuminated by a Herbig Be (B2/3Ve) star,

HD 200775 (The et al. 1994; Manoj et al. 2006). The whole cloud complex forms the hub and a single filament of nearly 5 pc in length, which runs toward the southwest with respect to the Galactic plane, providing a “head-tail” appearance to the whole cloud (Tachihara et al. 2002). Based on the *Gaia* Data Release 2 (DR2) parallax measurements of the young stellar objects (YSOs) associated with the cloud, Saha et al. (2020) estimated a distance of  $335 \pm 11$  pc to L1172/1174. Thus, L1172/1174 forms a relatively nearby cloud composed of a single long filament terminating at a hub where low- and intermediate-mass star formation is currently active in L1174, which is located to the northwest of HD 200775, and in L1172, which is located on the filament (e.g., Weston 1953; Kirk et al. 2009; Kun et al. 2009; Rector & Schweiker 2013; Yuan et al. 2013). Based on polarization measurements of more than 200 stars projected on the cloud in the *R* band, we determined the magnetic field geometry of the outer regions of the cloud complex. Apart from knowing the magnetic field orientation in the cloud complex, it is also interesting to study if there is any effect of HD 200775 on the ambient field orientation. Using the dust polarization in emission at submillimeter wavelengths obtained with the *Planck* satellite, we made a low resolution magnetic field map of the low- and high-density regions of the cloud complex and compared them with those inferred from our *R*-band polarization measurements to understand the orientation of the field lines with respect to the column density distribution. This paper is organized in the following manner. We describe the details of our observations and data reduction in Sect. 2. The polarization results are presented in Sect. 3, and we discuss our results in Sect. 4. Finally, we conclude our paper with a summary in Sect. 5.

## 2. Observations and data reduction

### 2.1. Polarization measurements in the *R* band

Polarimetric observations of 42 fields (each field is a circle of 8' in diameter) covering the cloud complex L1172/1174 were carried out using the ARIES Imaging Polarimeter (AIMPOL; Rautela et al. 2004). AIMPOL is mounted as a back-end instrument at the Cassegrain focus of the 1.04 m Sampurnanand Telescope, ARIES, Nainital, India. Only linear polarization can be obtained using AIMPOL, which consists of a half-wave plate (HWP) and a Wollaston prism. The HWP performs as a modulator and the Wollaston prism acts as a beam splitter, which splits the incoming light of each target into ordinary ( $I_o$ ) and extraordinary ( $I_e$ ) rays separated by  $\sim 28$  pixels (Eswaraiah et al. 2012). The CCD used during observations, is actually of  $1024 \times 1024$  pixel<sup>2</sup>, while frames for imaging polarimetry were obtained only within the central  $325 \times 325$  pixel<sup>2</sup> area. The plate scale of the CCD is 1.48 arcsec pixel<sup>-1</sup>. Rautela et al. (2004) provided a detailed description of AIMPOL. Each frame was obtained using a *R*-band filter ( $\lambda_{\text{eff}} = 0.760$   $\mu\text{m}$ ) by matching the Kron-Cousin passband. Table 2 in Saha et al. 2020 provides the log of the optical *R*-band polarimetric observations in the upper section. After bias subtraction, flat correction of the images using the flux normalization formula from Ramaprakash et al. (1998), we aligned and combined multiple images of an observed field.

We performed photometry of the selected pairs ( $I_o$  and  $I_e$  beams) of the observed sources using the Image Reduction and Analysis Facility (IRAF) DAOPHOT package to extract the fluxes of the  $I_o$  and  $I_e$  beams for individual sources. The selection of the  $I_o$  and  $I_e$  pair of each star from a given field is made automated using a program written in the Python language. The data reduction procedure is given in

Soam et al. (2013, 2015b, 2017). The details of our optical polarimetric observations were provided in our previous paper (Saha et al. 2020). The ratio  $R(\alpha)$  is given by

$$R(\alpha) = \frac{\frac{I_e(\alpha)}{I_o(\alpha)} - 1}{\frac{I_e(\alpha)}{I_o(\alpha)} + 1} = P \cos(2\theta - 4\alpha), \quad (1)$$

where  $P$  is the fraction of total linearly polarized light and  $\theta$  is the polarization angle of the plane of polarization. The  $\alpha$  is the position of the fast axis of the HWP at  $0^\circ$ ,  $22.5^\circ$ ,  $45^\circ$ , and  $67.5^\circ$  corresponding to four normalized Stokes parameters,  $q[R(0^\circ)]$ ,  $u[R(22.5^\circ)]$ ,  $q_1[R(45^\circ)]$ , and  $u_1[R(67.5^\circ)]$ , respectively. The polarization fraction  $P$  is estimated from  $\sqrt{q^2 + u^2}$  and the polarization angle,  $\theta = 0.5 \tan^{-1}(u/q)$ . Conventionally,  $\theta$  is measured with respect to the celestial north-south axis ( $0^\circ$  toward the north celestial pole and increasing toward the east). The uncertainties in normalized Stokes parameters  $\sigma_{R(\alpha)}$  ( $\sigma_q$ ,  $\sigma_u$ ,  $\sigma_{q_1}$  and  $\sigma_{u_1}$  in per cent) were estimated using the expression

$$\sigma_{R(\alpha)} = \frac{\sqrt{I_e + I_o + 2I_b}}{I_e + I_o}, \quad (2)$$

where  $I_b [= \frac{I_{bc} + I_{bo}}{2}]$  is the average background counts around the  $I_e$  and  $I_o$  beams of an observed source. The error in  $P\%$  and  $\theta$  are estimated using,

$$\sigma_P = \frac{1}{P} \times \sqrt{q^2 \sigma_q^2 + u^2 \sigma_u^2}, \quad \sigma_\theta = \frac{1}{2P^2} \times \sqrt{q^2 \sigma_u^2 + u^2 \sigma_q^2} \text{ rad}. \quad (3)$$

In order to determine the reference direction of the polarizer, we observed six polarized standard stars (HD 236633, BD+59°389, HD 19820, HD 204827, HD 25443, HD 15445) from the list given by Schmidt et al. (1992) during each observing run. Table 1 provides the optical  $R$ -band polarimetric results of the six polarimetric standard stars. HD204827 was observed in a single run. Mean degrees of polarization ( $P\%$ ) of HD 236633, BD+59°389, HD 19820, HD 25443, HD 15445 are 5.0, 6.1, 4.4, 4.8, 3.4 with standard deviations 0.2, 0.3, 0.2, 0.1, 0.2, respectively. Therefore, the estimated  $P\%$  of the observed standard stars are found to be comparable as provided by Schmidt et al. (1992). The difference between the computed  $\theta$  of individual standard star and its value given in Schmidt et al. (1992) was used to estimate the offset in the polarizer. Since 2004, the instrumental polarization of AIMPOL has been monitored by observing unpolarized standard stars, which is found to be stable (typically less than  $\sim 0.1\%$ ; see Rautela et al. 2004; Medhi et al. 2008; Eswaraiah et al. 2011; Soam et al. 2014, 2018a; Neha et al. 2016). Corrections for instrumental polarization were made for our polarimetric results.

## 2.2. Planck polarization measurements in submillimeter

Planck observed the whole sky in nine frequency bands (30–857 GHz) in total intensity, and up to 353 GHz in polarization (Planck Collaboration I 2014). The data were thus used to produce the first all-sky map of the polarized emission from dust at submillimeter wavelengths (Planck Collaboration I 2016). We used the intensity and polarization data only at 353 GHz as this is the highest frequency channel with polarization capabilities and the one with best signal-to-noise ratio (S/N) for dust polarization (Planck Collaboration Int. XIX 2015). We used the whole sky map (bandpass leakage corrected) at 353 GHz

**Table 1.** Polarized standard stars observed in the  $R$  band ( $\lambda_{\text{eff}} = 0.760 \mu\text{m}$ ).

Observing date	$P \pm \sigma_P$ (%)	$\theta \pm \sigma_\theta$ ( $^\circ$ )
HD 236633 ( <sup>a</sup> Standard values: $5.38 \pm 0.02\%$ , $93.^\circ 04 \pm 0.^\circ 15$ )		
11 Oct. 2015	$5.4 \pm 0.3$	$97 \pm 2$
3 Nov. 2015	$4.9 \pm 0.1$	$100 \pm 1$
15 Nov. 2015	$4.9 \pm 0.1$	$101 \pm 1$
16 Nov. 2015	$5.1 \pm 0.1$	$102 \pm 1$
17 Nov. 2015	$4.9 \pm 0.1$	$101 \pm 1$
15 Dec. 2015	$4.8 \pm 0.1$	$101 \pm 1$
23 Oct. 2016	$5.2 \pm 0.1$	$100 \pm 1$
25 Oct. 2016	$5.0 \pm 0.1$	$99 \pm 1$
26 Oct. 2016	$4.8 \pm 0.1$	$98 \pm 1$
27 Oct. 2016	$4.9 \pm 0.1$	$100 \pm 1$
13 Oct. 2017	$4.9 \pm 0.2$	$102 \pm 1$
19 Oct. 2017	$5.1 \pm 0.2$	$100 \pm 1$
20 Oct. 2017	$5.0 \pm 0.2$	$101 \pm 1$
21 Oct. 2017	$5.3 \pm 0.2$	$102 \pm 1$
26 Oct. 2017	$5.1 \pm 0.2$	$101 \pm 1$
27 Oct. 2017	$4.9 \pm 0.1$	$100 \pm 1$
BD+59°389 ( <sup>a</sup> Standard values: $6.43 \pm 0.02\%$ , $98.^\circ 14 \pm 0.^\circ 10$ )		
11 Oct. 2015	$6.2 \pm 0.2$	$104 \pm 1$
2 Nov. 2015	$6.4 \pm 0.1$	$106 \pm 1$
3 Nov. 2015	$6.3 \pm 0.1$	$105 \pm 1$
15 Nov. 2015	$6.0 \pm 0.1$	$106 \pm 1$
16 Nov. 2015	$6.4 \pm 0.1$	$106 \pm 1$
17 Nov. 2015	$6.2 \pm 0.1$	$106 \pm 1$
25 Oct. 2016	$6.0 \pm 0.1$	$104 \pm 1$
28 Oct. 2016	$5.6 \pm 0.1$	$105 \pm 1$
22 Nov. 2016	$6.3 \pm 0.1$	$106 \pm 1$
27 Nov. 2016	$6.4 \pm 0.3$	$109 \pm 1$
13 Oct. 2017	$5.9 \pm 0.1$	$106 \pm 1$
14 Oct. 2017	$6.4 \pm 0.1$	$107 \pm 1$
17 Oct. 2017	$5.7 \pm 0.2$	$106 \pm 1$
18 Oct. 2017	$5.7 \pm 0.2$	$107 \pm 1$
19 Oct. 2017	$6.0 \pm 0.2$	$107 \pm 1$
20 Oct. 2017	$6.1 \pm 0.2$	$107 \pm 1$
21 Oct. 2017	$6.9 \pm 0.2$	$105 \pm 1$
26 Oct. 2017	$6.0 \pm 0.2$	$103 \pm 1$
HD 19820 ( <sup>a</sup> Standard values: $4.526 \pm 0.025\%$ , $114.^\circ 46 \pm 0.^\circ 16$ )		
15 Dec. 2015	$4.6 \pm 0.1$	$123 \pm 1$
22 Nov. 2016	$4.3 \pm 0.1$	$126 \pm 1$
26 Nov. 2016	$4.2 \pm 0.1$	$124 \pm 1$
HD 204827 ( <sup>a</sup> Standard values: $4.893 \pm 0.029\%$ , $59.^\circ 10 \pm 0.^\circ 17$ )		
23 Oct. 2016	$4.7 \pm 0.1$	$66 \pm 1$
HD 25443 ( <sup>a</sup> Standard values: $4.734 \pm 0.045\%$ , $133.^\circ 65 \pm 0.^\circ 28$ )		
26 Nov. 2016	$4.7 \pm 0.2$	$143 \pm 1$
27 Nov. 2016	$4.8 \pm 0.2$	$143 \pm 1$
HD 15445 ( <sup>a</sup> Standard values: $3.683 \pm 0.072\%$ , $88.^\circ 91 \pm 0.^\circ 56$ )		
22 May 2017	$3.6 \pm 0.2$	$107 \pm 2$
23 May 2017	$3.2 \pm 0.2$	$102 \pm 2$

**Notes.** (<sup>a</sup>)Values in the  $R$  band from Schmidt et al. (1992).



provided by *Planck* Legacy Archive<sup>1</sup>. The polarization of the cosmic microwave background (CMB) has a negligible contribution to the sky polarization toward the molecular clouds at 353 GHz (*Planck Collaboration Int. XXX 2016*). So, CMB polarization was not taken into account in our analysis. The  $I$ ,  $Q$ , and  $U$  maps analyzed here have been constructed using the gnomonic projection of the HEALPix<sup>2</sup> (*Górski et al. 2005*) all-sky maps. We used *healpy* (*Zonca et al. 2019*) to extract and analyze data for calculation of  $P\%$  and  $\theta$ . *healpy* is a Python package to handle pixelated data on the sphere.

We estimated the Stokes  $I$ ,  $Q$ , and  $U$  parameters from the smoothed *Planck* map of a  $8^\circ$  square area obtained from the *Planck* 353 GHz image centered at HD 200775. The Stokes parameter maps are shown in accordance with the IAU convention (i.e., the polarization angle  $\psi = 0^\circ$  toward the Galactic north, increasing toward the Galactic east) (*Hamaker & Bregman 1996*). The angle of the magnetic field projected on the sky plane can be obtained by adding  $90^\circ$  to the polarization angle ( $\psi + 90^\circ$ ). At 353 GHz, the *Planck* data have an angular resolution of  $4.8'$ .

### 2.3. $^{12}\text{CO}$ (1–0) molecular line observations using TRAO

As a part of a comprehensive study of L1172/1174 to understand the gas dynamics (*Sharma et al. 2021*, under preparation), the whole cloud of L1172/L1174 was observed in  $^{12}\text{CO}$ ,  $\text{C}^{18}\text{O}$ ,  $\text{N}_2\text{H}^+$  (1–0), and CS (2–1) transitions using the on-the-fly (OTF) mapping technique and the 14 m diameter single-dish telescope of Taedeuk Radio Astronomy Observatory (TRAO) in Daejeon, South Korea, between November 16–28, 2018. Here we present only the  $^{12}\text{CO}$  line results mainly to estimate the magnetic field strengths in the cloud using the  $^{12}\text{CO}$  linewidths. The back-end system with fast Fourier transform spectrometer has  $4096 \times 2$  channels at 15 kHz resolution ( $\sim 0.05 \text{ km s}^{-1}$  at 110 GHz). The typical rms noise in one channel was  $\sim 0.35 \text{ K}$  for  $^{12}\text{CO}$  lines in  $T_{\text{A}}^*$  scale. At 115 GHz the beam size (HPBW) of the telescope is about  $47''$  and the fraction of the beam pattern subtending main beam (beam efficiency) is  $41 \pm 2\%$  (*Jeong et al. 2019*). The system temperature was 550 K–600 K during the observations. The spectra were reduced using CLASS software of the IRAM GILDAS software package.

### 2.4. Archival Gaia DR2

*Gaia* DR2 presents positions, parallaxes, and proper motions of more than a billion objects (*Gaia Collaboration 2018*) with unprecedented precision. Typical uncertainties in parallax measurements of sources brighter than  $\sim 14 \text{ mag}$  are around 0.4 mas. Sources having  $G$ -mag around 17 have typical uncertainties  $\sim 0.1 \text{ mas}$  and  $\sim 0.7 \text{ mas}$  for faint sources ( $G$ -mag around 20) (*Luri et al. 2018*). But if the relative uncertainties in parallax values were  $\geq 20\%$ , the corresponding distances would not follow the simple inversion of their parallaxes (*Bailer-Jones 2015*). Recently, *Bailer-Jones et al. (2018)* provided a probabilistic estimate of the stellar distances from the parallax measurements in *Gaia Collaboration (2018)*, using an exponentially decreasing space density prior that is based on a galactic model. In our analysis, the stellar distances were obtained from *Bailer-Jones et al. (2018)*, by giving a search around a circle of radius of  $1''$  around the source positions.

<sup>1</sup> <http://www.cosmos.esa.int/web/planck/pla/>

<sup>2</sup> <http://healpix.sourceforge.net>

**Table 2.** Polarimetric results of the YSO candidates.

ID	$l$ ( $^\circ$ )	$b$ ( $^\circ$ )	$P_{\text{R}} \pm \sigma P_{\text{R}}$ (%)	$\theta_{\text{R}} \pm \sigma \theta_{\text{R}}$ ( $^\circ$ )
3	104.041838	14.259696	$1.4 \pm 0.6$	$156 \pm 10$
13/13b <sup>(*)</sup>	104.029883	14.063977	$2.6 \pm 0.3$	$182 \pm 3$
18	104.372912	14.192269	$2.6 \pm 0.6$	$202 \pm 6$
27	104.036152	14.301923	$2.9 \pm 0.7$	$181 \pm 7$

**Notes.** <sup>(\*)</sup>This source appeared as double sources in *Gaia* DR2 (LkHa 428 N/S; *Kun et al. 2009*).

## 3. Results

### 3.1. Optical and submillimeter polarization

Although the Stokes parameters  $Q$  and  $U$  can be both positive or negative, the polarization  $P$  derived from these parameters is always positive and thus it has a positive bias, especially for sources with low S/Ns. In order to eliminate this bias, we estimated the debiased  $P$  using  $P = \sqrt{P^2 - \sigma_{\text{P}}^2}$ , where  $\sigma_{\text{P}}$  is the error in  $P$  (*Wardle & Kronberg 1974*). There are 301 sources for which the ratios of the  $P\%$ ,  $\theta_{\text{P}}$ , and distance to their corresponding errors,  $P/\sigma_{\text{P}}$ ,  $\theta_{\text{P}}/\sigma_{\theta_{\text{P}}}$ , and  $d/\sigma_{\text{d}}$ , respectively, are greater than three. Of the 301 sources, we included 249 of them, which show uncertainty in polarization measurement  $\leq 1\%$ . This corresponds to a *Gaia*  $G$  magnitude brighter than  $\sim 17$ . Though we have polarimetric results for four YSO candidates located toward L1172/1174, these sources are not included in our analysis as there could be additional effects on polarization measurements due to possible presence of circumstellar dust (e.g., *Strom 1977*; *Elsasser & Staude 1978*; *Bastien & Landstreet 1979*; *Bastien 1982, 1985*; *Sato 1988*; *Ménard 2005*; *Vink et al. 2005*). These sources are shown separately in Table 2. The YSO candidates with IDs 3, 13/13b, and 18 are detected in *Gaia* DR2 and hence were listed in Table 3 of *Saha et al. (2020)*. The last source (ID 27) has no detection in *Gaia* DR2, and therefore it was listed in Table 7 of *Saha et al. (2020)*. In Fig. 1a we show the results from our  $R$ -band polarization measurements (lines shown in yellow) of 249 stars. Table A.1 lists the polarimetric measurements of these stars. The lengths and orientations of the polarization vectors correspond to the degree of polarization ( $P_{\text{R}}$ ) in per cent and the position angle ( $\theta_{\text{R}}$ ) in degree measured from the north to east, respectively. The polarization vectors are plotted over the  $\sim 2^\circ$  hydrogen column density map made using the images obtained with the *Herschel* satellite (*André et al. 2010*). The median value of the column density toward the 249 stars observed by us is found to be  $9 \times 10^{20} \text{ cm}^{-2}$ . The outermost contour in Fig. 1a is drawn at this level, which corresponds to an extinction of  $\sim 1$  magnitude converted using the relationship between the column density and the extinction derived by *Bohlin et al. (1978)*.

Interstellar polarization due to the differential extinction of starlight by the asymmetric dust grains aligned with the ambient magnetic field was reported more than half a century ago (*Hall 1949*; *Hiltner 1949*). For years, a number of grain alignment paradigms have been proposed. As the dust grains are composed of paramagnetic material, they contain unpaired electrons. Through the Barnett effect they can develop an internal magnetization (*Dolginov & Mitrofanov 1976*). Due to the presence of magnetic field, the directions of angular momentum of these magnetized dust grains are aligned along the direction of field lines via the continuing radiative torques

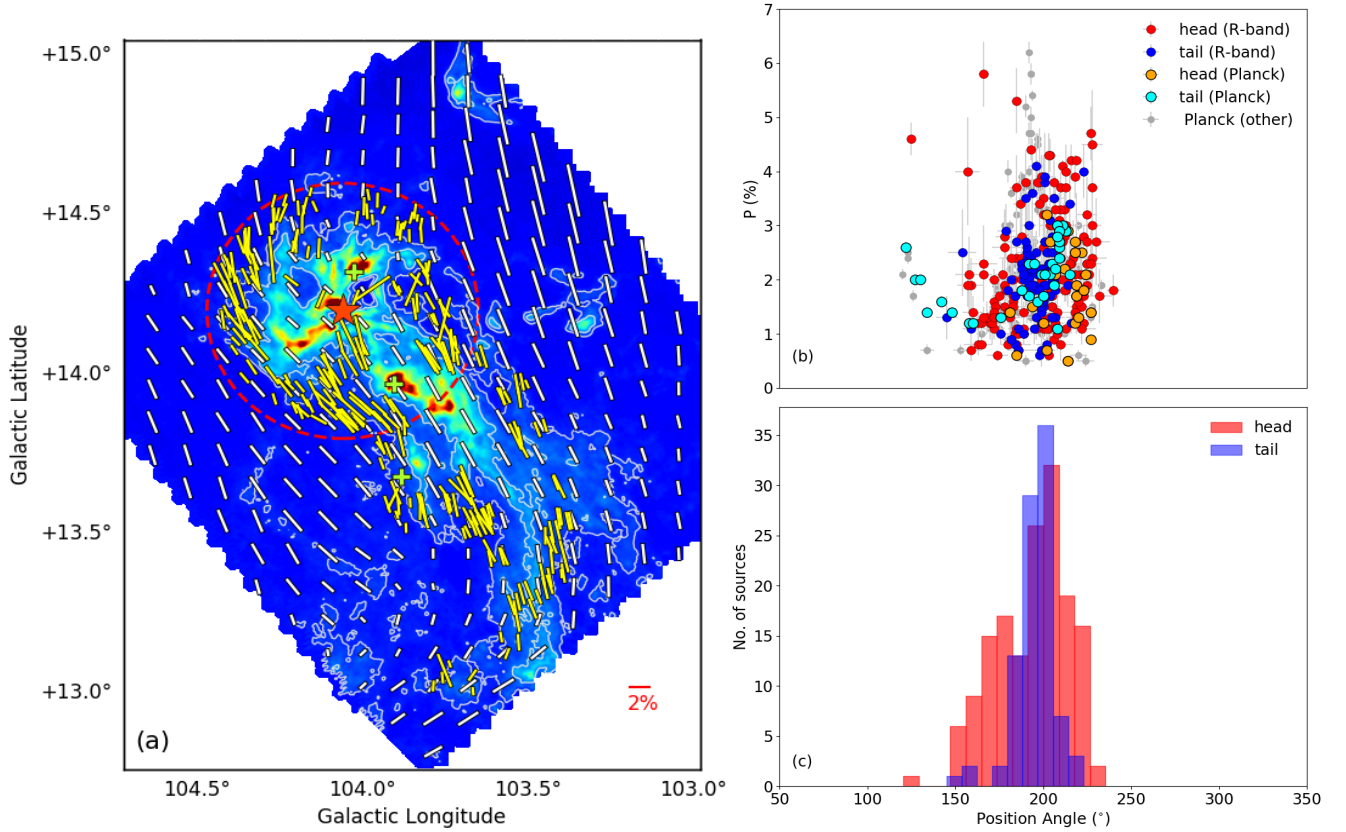


**Fig. 1.** Polarimetric results obtained toward the L1172/1174 cloud complex. (a) *R*-band (yellow) and *Planck* (white) polarization vectors ( $90^\circ$  rotated) overlaid on the *Herschel* dust column density map of L1172/1174 obtained from André et al. (2010). The contours are drawn at  $9 \times 10^{20} \text{ cm}^{-2}$  and  $15 \times 10^{20} \text{ cm}^{-2}$  levels to reveal the cloud structure. HD 200775 is marked with a red star symbol. The dashed red circle represents the head region of the cloud complex. The green colored plus symbols show the locations of L1173 (south), L1172 (middle), and L1174 (north). The lengths and the orientations of the vectors correspond to the degree of polarization and the position angles measured with respect to the Galactic north increasing eastward, respectively. A polarization vector (red) corresponding to 2% and oriented at  $90^\circ$  is shown for reference. (b) Plot of degree of polarization versus position angle values for the 249 sources observed by us in the *R* band and *Planck*. The *R*-band polarization vectors from the head and the tail regions are shown using solid red and blue circles, respectively. Similarly, for *Planck*, the measurements from the head and the tail regions are shown using solid orange and cyan circles, respectively. The *Planck* polarization measurements from the ICM are shown with solid gray circles. (c) Histograms of the  $\theta_R$  belonging to the head and the tail regions of L1172/1174 obtained from our *R*-band polarization measurements with the bin size of  $\sim 9^\circ$ .

over the period of Larmor precession. According to Davis & Greenstein (1951), on account of paramagnetic losses by dissipation of the angular momentum components perpendicular to magnetic field direction, the dust grains get aligned with field lines. Another mechanism was proposed based on mechanical grain alignment (Gold 1952a,b). However, a majority of theoretical and observational studies indicated the mechanism of radiative alignment torque (RAT), which became the best to explain the interstellar polarization. This mechanism was first introduced by Dolginov & Mitrofanov (1976) and later studied by Draine & Weingartner (1996, 1997). Lazarian & Hoang (2007) formulated the analytical model of RAT paradigm. According to RAT theory, the aspherical dust grains rotate due to radiative torque and orient with their long axes perpendicular to magnetic field lines (B-RAT; Lazarian & Hoang 2007). In another scenario of RAT mechanism, *k*-RAT (significant in the vicinities of bright stars), the dust grains precess about the direction of radiation (Lazarian & Hoang 2007; Tazaki et al. 2017). The selective extinction due to the aligned, elongated dust grains builds the polarization vectors oriented along the direction of the plane-of-sky component of the magnetic field ( $B_{\text{POS}}$ ). Now, the thermal continuum emission would be polarized along the long axes of the elongated dust grains, which is perpendicular to the

field direction. Therefore, the polarization vectors deduced by submillimeter emission have to be rotated by  $90^\circ$  to estimate the geometry of the  $B_{\text{POS}}$  (Goodman 1996; Wolf et al. 2003).

In Fig. 1a, the *Planck* polarization vectors are presented, which are  $90^\circ$  rotated by their original orientations to indicate the magnetic field directions. Here again, the lengths and orientations of the polarization vectors correspond to the degree of polarization ( $P_p$ ) and the position angle ( $\theta_p$ ) in degree measured from the north toward the east, respectively. For the purpose of analysis, *R*-band polarization vectors lying within a circular region of  $0.4^\circ$  (the extent over which we have *R*-band polarization across the cloud complex) radius around HD 200775 are considered as part of the head and those lying outside of this region are considered as part of the tail region. The  $P_R$  and the  $\theta_R$  for the sources lying toward the head and the tail regions are shown in Fig. 1b. The results of  $P_R$  and  $\theta_R$  in both head and tail regions are presented in Table 3. The median absolute deviations (MADs), more resilient to outliers in a data set, of  $P_R$  and  $\theta_R$  are also listed as uncertainties. The histograms of  $\theta_R$  from the head and the tail regions are shown in Fig. 1c.

The *Planck* polarization measurements,  $P_p$  and  $\theta_p$ , for the head and the tail regions are also shown in Fig. 1b. Here, the *Planck* polarization vectors that fall within the  $9 \times 10^{20} \text{ cm}^{-2}$

**Table 3.** Polarimetric results in head and tail of L1172/1174 and ICM.

Region	Range		Median	
	$P$ (%)	$\theta$ ( $^\circ$ )	$P$ (%)	$\theta$ ( $^\circ$ )
Optical $R$ -band polarimetric results				
Head	0.6–5.8	125–240	$2.1 \pm 0.7$	$203 \pm 15$
Tail	0.6–4.1	145–223	$2.0 \pm 0.4$	$196 \pm 6$
<i>Planck</i> polarimetric results				
Head	0.5–3.2	181–227	$1.8 \pm 0.6$	$218 \pm 6$
Tail	1.1–3.0	122–215	$2.1 \pm 0.5$	$201 \pm 8$
ICM	0.5–6.2	120–233	$2.2 \pm 0.7$	$195 \pm 11$

contour are considered as associated with the cloud complex and those lying outside (but within the *Herschel* field) are considered as polarization from the ICM. Of the measurements falling within the  $9 \times 10^{20} \text{ cm}^{-2}$  contour, those lying within the circular region of  $0.4^\circ$  radius are considered as the part of the head region while those falling outside the circular region of  $0.4^\circ$  radius are considered as the part of the tail. The number of data points is lesser compared to the  $R$ -band polarization due to the coarse resolution of the *Planck* measurements. We used the threshold of  $P/\sigma_P > 3$  in the analysis of *Planck* data as well. The *Planck* polarization measurements were debiased using the equations given by Montier et al. (2015). The uncertainties of  $P_P$  and  $\theta_P$  are estimated using the equations provided by Montier et al. (2015). Typical uncertainties in the measurements of  $P_P$  and  $\theta_P$  are found to be 0.1% and  $1^\circ$ , respectively. The results of  $P_P$  and  $\theta_P$  in both head and tail regions of the cloud complex and also in the ICM are presented in Table 3.

### 3.2. $^{12}\text{CO}$ gas distribution in L1172/1174 complex

The  $^{12}\text{CO}$  velocity for the entire cloud complex ranges from  $-2.8 \text{ km s}^{-1}$  to  $7.8 \text{ km s}^{-1}$ . The average full width at half maximum (FWHM) of the  $^{12}\text{CO}$  is found to be  $\sim 2.0 \text{ km s}^{-1}$ . The cavity surrounding HD 200775 is conspicuous with high intensity peaks located along the rim of the cavity. The  $^{12}\text{CO}$  is found to show gas structures, especially to the east and west of HD 200775, where the gas components in the velocity range of  $-2.5$ – $0 \text{ km s}^{-1}$  and  $5.0$ – $7.5 \text{ km s}^{-1}$ , respectively are located, supporting the earlier reporting of the presence of bipolar outflow lobes (Watt et al. 1986). The  $V_{\text{lsr}} = 2.65 \text{ km s}^{-1}$  of the cloud complex is determined from the  $N_2\text{H}^+$  line detected in the cores (Sharma et al. 2021, under preparation). The  $V_{\text{lsr}}$  is computed as a mean of L1174 ( $2.5 \text{ km s}^{-1}$ ) and L1172 ( $2.8 \text{ km s}^{-1}$ ) regions. Multiple velocity components in the  $^{12}\text{CO}$  line profiles are found in different parts of the cloud complex. The gas dynamics of the region surrounding HD 200775 will be presented in a subsequent article (Sharma et al. 2021, under preparation). In this work, we used the  $^{12}\text{CO}$  linewidths to calculate the strength of the  $B_{\text{POS}}$ .

## 4. Discussion

### 4.1. Magnetic field geometry of the L1172/1174 complex

Interstellar dust grains produce extinction of light from the background stars as well as emit thermal radiation. When the unpolarized starlight impinges on a series of aspherical dust grains, the electromagnetic wave is absorbed maximum along the long axis of grain. The transmitted radiation is parallel to the short axis and becomes partially plane polarized, oriented along the  $B_{\text{POS}}$  (Whittet 2005). On the other hand, thermal emission from the dust grains is maximum along the longer axis, thus

becomes polarized perpendicular to  $B_{\text{POS}}$ . Since dust grains are coupled with the magnetic field, measurements of dust polarization provide information on the structure and the strength of the magnetic field. The value of position angle depends on the orientation of the  $B_{\text{POS}}$  and the efficiency of the dust grain alignment with the field. It also depends on the variation in the orientation of  $B_{\text{POS}}$  along the line-of-sight (Lee & Draine 1985). The polarization measurements in the optical bands trace the  $B_{\text{POS}}$  only in the outskirts of the molecular clouds where the extinction ( $A_V$ ) is relatively low (Guetter & Vrba 1989; Harjunpää et al. 1999). On the other hand, the polarization measurements in submillimeter or millimeter can infer the  $B_{\text{POS}}$  inside the cloud where  $A_V$  is relatively high (e.g., Hildebrand et al. 1984; Goodman 1995; Greaves et al. 1999).

The measured polarization in optical wavelengths is caused by the dust grains that are lying all along the light of sight (within the pencil beam) between the star and us. Though the dust grains present within the cloud are mostly responsible for the observed polarization, those that are present foreground to the cloud can also contribute. To infer the amount of polarization caused by the dust grains within the cloud (thus the magnetic field geometry), it is necessary to remove the foreground component. Generally, the stars located foreground to the cloud are used to estimate the foreground component of the polarization. The  $P_R$  versus distance and  $\theta_R$  versus distance plots of the observed sources are shown in Figs. 3a,b in Saha et al. (2020), respectively, using solid gray triangles (in equatorial coordinate system). The sources having  $G$  magnitudes fainter than  $\sim 17$  were also included in that figure. Among the stars observed by us, only one star, located at 306 pc, is foreground to the cloud. Therefore, we searched in Heiles (2000) catalog to get more foreground sources having polarization measurements. The search was made within a circular region of  $6^\circ$  radius about HD 200775. We obtained a total of 26 sources around HD 200775. In our analysis, we discarded four sources, HD 200775, HD 193533, HD 208947 and HD 203467 (reason for not considering these sources was explained in Saha et al. 2020). Of the remaining 22, we obtained the *Gaia* DR2 distance for 17 sources from the Bailer-Jones et al. (2018) catalog.

The degree of polarization ( $P_H$ ) in per cent and polarization position angles ( $\theta_H$ ) in degree of the 17 sources are also shown using filled circles in black in both a and b of Fig. 3 of Saha et al. (2020), respectively. As the foreground sources show significantly low degree of polarization, we set no constraints on the  $P/\sigma_P$  values during their selection. Of the 17 sources, 13 sources are found to be located at distances less than 335 pc (distance of L1172/1174) and four sources are at distances greater than 335 pc. The mean values of  $P_H$  and  $\theta_H$  for the 13 foreground sources are found to be 0.1% and  $122^\circ$ , respectively and the corresponding mean values for the four background sources are found to be 1.9% and  $199^\circ$ , respectively. Both  $P_H$  and  $\theta_H$  values of the four background sources are found to be consistent with the values of the sources observed by us toward L1172/1174. Using the mean values of  $P_H$  and  $\theta_H$  obtained for the 13 stars, we calculated the mean Stokes parameters  $Q_{\text{fg}} (= P \cos 2\theta)$  and  $U_{\text{fg}} (= P \sin 2\theta)$  as  $-0.043$  and  $-0.089$ , respectively. We subtracted these values from the Stokes parameters of the observed stars vectorially to calculate the foreground-corrected percentage of polarization ( $P_c$ ) and the position angle ( $\theta_c$ ) values. No significant changes are noticed in the results after correcting for the foreground polarization. As a result, the  $R$ -band polarization vectors (in yellow) presented in Fig. 1a represent the  $B_{\text{POS}}$  geometry toward the periphery of L1172/1174 complex.



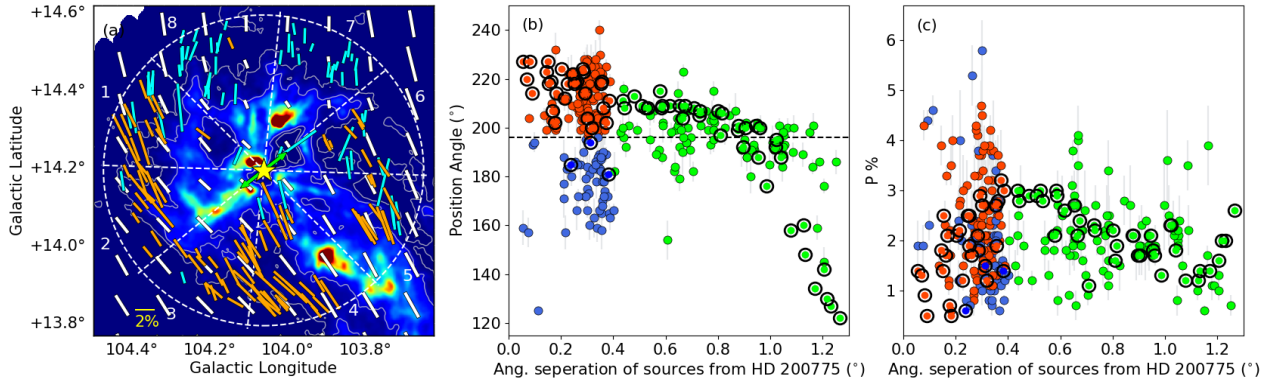


**Fig. 2.** Variation in the projected magnetic field geometry toward the L1172/1174 cloud complex. (a) Optical  $R$ -band and *Planck* polarimetric results overlaid on *Herschel* column density map. Location of HD 200775 (yellow star) is also shown. The green colored arrows imply the directions of outflow from HD 200775. The eight sectors are indicated using dashed white lines and also marked. Orange lines indicate the polarization measurements in the  $R$  band with  $\theta_R \geq 196^\circ$  and cyan lines represent the same with  $\theta_R < 196^\circ$ . White lines represent *Planck* polarimetric results with  $90^\circ$  rotation. A polarization vector corresponding to 2% is shown for reference. (b) Variation in the  $\theta_R$  of the sources with respect to the angular separation from HD 200775. Upto  $0.4^\circ$  (Sects. 1–8) there are sources located toward the head region with two sets of distribution of position angles  $\sim 211^\circ$  (red filled circles, shown in orange lines in (a)) and  $\sim 179^\circ$  (blue filled circles, shown in cyan lines in (a)). The green filled circles are the sources distributed toward the tail region. The dashed horizontal line indicates the mean  $\theta_R$  value ( $\sim 196^\circ$ ) of the same sources. Position angles obtained from *Planck* observations are shown using thick open black circles (shown in white lines in (a)). (c) Variation in the  $P_R\%$  and  $P_P\%$  with respect to the angular separation from HD 200775. The symbols represent the same as described in panel b.

As evident from Figs. 1a,b, the orientations of  $B_{\text{POS}}$  obtained from the  $R$  band ( $\theta_R = 203^\circ$  for the head and  $\theta_R = 196^\circ$  for the tail) and *Planck* ( $\theta_P = 212^\circ$  for the head and  $\theta_P = 200^\circ$  for the tail) observations are found to be in good agreement all along the structure of the cloud complex. Such correlations between the magnetic field geometries inferred from the optical and the *Planck* polarization measurements are reported in a number of studies (e.g., Soler et al. 2016; *Planck* Collaboration Int. XXXV 2016; Gu & Li 2019). This implies that the magnetic fields inferred from the *Planck* polarization and from the  $R$ -band polarization measurements toward the high-density parts and toward the outer envelope of L1172/1174, respectively, are well correlated with each other. Though consistent with the *Planck* measurements, small-scale substructures in the magnetic field toward the envelope region can be noticed in the  $R$ -band polarimetric results. The substructures do not appear in the *Planck* measurements as *Planck* traces the large-scale component of the magnetic field. Also, due to the relatively poor resolution, the *Planck* data could not reveal any effect on the magnetic field by the local kinematics and overall substructures at high-density regimes. Even the *Planck* polarization vectors from outside of the  $9 \times 10^{20} \text{ cm}^{-2}$  contour that represent the  $B_{\text{POS}}$  in ICM ( $\theta_{\text{ICM}} = 190^\circ$ ) are correlated with both  $\theta_R$  and  $\theta_P$  implying that the cloud  $B_{\text{POS}}$  is threaded by the ICM  $B_{\text{POS}}$  surrounding the cloud.

In Fig. 2a we show the  $B_{\text{POS}}$  geometry of the head region of L1172/1174 inferred from our  $R$ -band and the *Planck* polarization results. In Figs. 2b,c we show the  $\theta_R$  and  $P_R$  values of the stars as a function of their angular separation from HD 200775, respectively. The *Planck* polarimetric values ( $\theta_P$  and  $P_P$ ) are also shown in the same figures. The primary goal here is to investigate whether the presence of HD 200775 has any effect on the magnetic field geometry around it. Two components of  $B_{\text{POS}}$  ( $\theta_R \geq 196^\circ$  and  $< 196^\circ$ ) are apparent in Fig. 2b for the sources lying toward the head region. The changes in the  $\theta_R$  and  $\theta_P$  found beyond  $\sim 1^\circ$  toward the tail are due to the curved geometry of  $B_{\text{POS}}$ , which is found to correlate well with the geometry of the cloud structure there. The median values of  $\theta_R$  lying toward the head region and having  $\theta_R \geq 196^\circ$  and  $< 196^\circ$  are found to be

$211^\circ$  and  $179^\circ$  respectively with the MAD of  $8^\circ$  for both the distributions. The distribution of  $\theta_R$  in Fig. 2b actually reflects the distribution of the magnetic field vectors on the cloud as shown in Fig. 2a with  $179^\circ$  component lying predominantly to the north-western parts of HD 200775 and the  $211^\circ$  component lying to the southeastern parts. Similar to Fig. 2b, a clear bimodal angle distribution ( $\theta_R \geq 196^\circ$  and  $< 196^\circ$ ) of the histogram of  $\theta_R$  in head region can be noticed in Fig. 1c. As evident from that figure, the histogram of  $\theta_R$  in the tail peaks at the median  $\theta_R$  ( $196^\circ$ ), almost overlapping with the higher  $\theta_R$  values ( $\geq 196^\circ$ ), which is noticeable in Fig. 2b also. Figure 2c is similar to Fig. 1b, which shows that  $P_P$  values are similar to the  $P_R$  values. While we obtained the bimodal distribution both in  $\theta_P$  and  $\theta_R$ , there is no such bimodality present in  $P_P$  and  $P_R$ .

The four observed YSO candidates in Table 2 are all found to be located toward the head region. As evident from Figs. 1b,c, the polarimetric results of all the YSO candidates are found to be consistent with other observed stars. The  $P_R$  and  $\theta_R$  of YSO candidates agree well with the median values of the same in the head region of Table 3, except the  $\theta_R$  of star ID 3. However, the latter falls well within the range of  $\theta_R$  of the head region. Except star ID 18 in Table 2,  $\theta_R$  of other YSO candidates fall on the group of lower  $\theta_R$  ( $< 196^\circ$ ) values.

To investigate the variation in the projected magnetic field orientations in more detail, we divided the head region into 8 equal sectors drawn within the circular area of  $0.4^\circ$  radius centered at HD 200775 as shown in Fig. 2a. The division of the region is made with respect to the symmetry axis of the outflow cavity believed to have been carved out by HD 200775 (Fuente et al. 1998). The star formation process is ongoing mainly in this circular region. The median values of  $P_R$  (Col. 2),  $\theta_R$  (Col. 3) and the MAD (Col. 4) of the  $\theta_R$  for each sector are given in Table 4. The component showing the median value of  $211^\circ$  is dominant toward the sectors 2, 3, and 4, which lie to the south and south-east of HD 200775. The median value of  $P_R$  for this component is 2.4%. The component showing the median value of  $179^\circ$  is largely distributed toward sectors 7 and 8, which lie to the north of HD 200775. The median value of  $P_R$  for this component is 1.6%, which is relatively low ( $\sim 2\sigma$ ). Sectors 1, 5, and 6 show the

**Table 4.**  $P_R$ ,  $\Delta\theta$ ,  $\Delta V$ ,  $n_{H_2}$ , and  $B_{POS}$  in different sectors of L1172/1174 cloud complex.

Id <sup>(†)</sup>	$P_R^{(*)}$ (%)	$\theta_R^{(*)}$ (°)	$\Delta\theta_R^{(*)}$ (°)	$\Delta V$ (kms <sup>-1</sup> )	$n_{H_2}$ (cm <sup>-3</sup> )	$B_{POS}$ ( $\mu G$ )
(1)	(2)	(3)	(4)	(5)	(6)	(7)
1	2.6 ± 0.7	198 ± 8	6 ± 2	2.2 ± 0.2	93 ± 38	33 ± 13
2	2.2 ± 0.8	213 ± 7	6 ± 2	2.1 ± 0.1	91 ± 37	31 ± 12
3	2.2 ± 0.8	212 ± 7	5 ± 2	1.8 ± 0.1	90 ± 36	32 ± 14
4	2.7 ± 0.6	219 ± 8	7 ± 1	2.2 ± 0.2	101 ± 40	29 ± 8
5	3.3 ± 0.8	200 ± 11	10 ± 1	1.3 ± 0.2	121 ± 49	13 ± 4
6	2.0 ± 0.4	200 ± 13	12 ± 1	1.5 ± 0.1	70 ± 28	10 ± 2
7	1.4 ± 0.3	174 ± 8	6 ± 2	2.1 ± 0.1	67 ± 27	27 ± 10
8	1.3 ± 0.5	178 ± 8	6 ± 2	1.8 ± 0.1	93 ± 37	27 ± 11
tail	2.0 ± 0.4	196 ± 6	4 ± 1	1.7 ± 0.2	113 ± 45	42 ± 14

**Notes.** <sup>(†)</sup>The identification numbers of sectors 1–8 as shown in Fig. 2a. <sup>(\*)</sup>Optical  $R$ -band measurements.

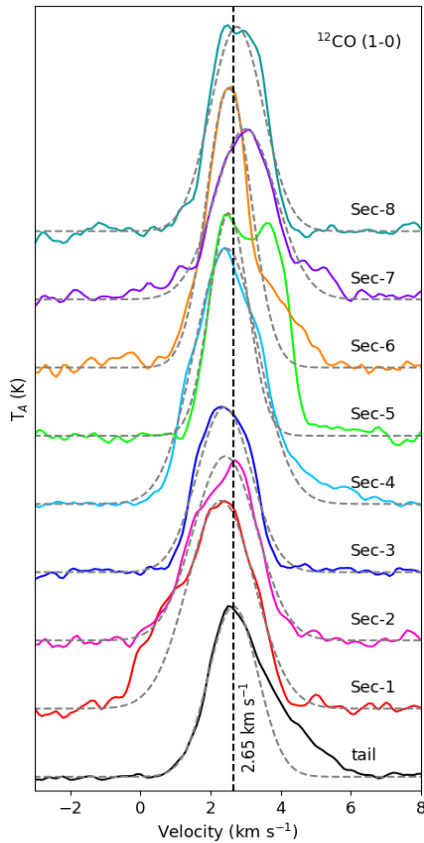


**Fig. 3.** Average  $^{12}CO$  ( $J = 1-0$ ) line profiles for the eight sectors made toward the head. The average  $^{12}CO$  ( $J = 1-0$ ) line profile for the tail region is shown in black. The  $V_{lsr} = 2.65$  km s<sup>-1</sup> is shown using a dashed vertical line. The dashed curves are the Gaussian fitted lines used to obtain the  $\Delta V$ .

presence of both the components. The median value of the  $\theta_R$  in these three regions is found to be  $\sim 200^\circ$ , which is roughly the average of the two ( $179^\circ$  and  $211^\circ$ ) components. The deviation in the  $\theta_R$  ( $\Delta\theta_R$ ) is found to be the lowest toward the tail region and highest toward sectors 5 and 6.

In Fig. 3 we show the average  $^{12}CO$  ( $J = 1-0$ ) line profiles for the eight sectors identified toward the head region. The  $^{12}CO$  lines toward the lines-of-sight of the stars for which we have

$R$ -band polarization measurements are used for getting the average profiles. The average  $^{12}CO$  line profile for the tail region is also shown in Fig. 3. The measurements having  $S/N \geq 3$  are used for generating the average profiles. The estimated  $V_{lsr}$  ( $=2.65$  km s<sup>-1</sup>) of the cloud complex is also identified with a vertical line to show the presence of redshifted and blueshifted velocity components in different sectors. The  $^{12}CO$  line toward the tail region is found to be peaking at the  $V_{lsr}$  velocity with a FWHM ( $\Delta V$ ) value of  $1.7$  km s<sup>-1</sup> obtained from a Gaussian fit to the profile. However, the profile shows a line profile skewed to the redder velocities, which is more likely to be due to the presence of high-velocity (both blue- and red-shifted) gas.

The average  $^{12}CO$  line profiles for sectors 3, 4, and 7 are found to be consistent with a Gaussian shape, though presence of high-velocity components are seen toward most of the sectors similar to what we observed toward the tail region. While the line peaks toward sectors 1, 3, 4, and 5 are shifted toward the bluer velocities, the line toward sector 7 shows a shift toward the redder velocity with respect to the  $V_{lsr}$ . Sectors 2 and 6 are found to peak at the  $V_{lsr}$  velocity. The line profiles at sectors 1 and 2 show additional components at bluer velocities, whereas a relatively narrow linewidth with high-velocity wings to the redder velocities are seen for the profile in sector 6. Compared to other sectors, sector 5 shows distinct profile with an additional velocity component to the redder side of the line center having both the peaks with comparable intensity. Thus, for sector 5, we fitted the observed line profile with the two Gaussian components and the linewidth ( $\Delta V \approx 1.3$  km s<sup>-1</sup>) corresponding to the component closest to the  $V_{lsr}$  is used to estimate the magnetic field strength.

It is observed that the high-velocity gas is not widespread but localized. It is possible that the high-velocity gas present toward, especially, sectors 5 and 6 may be responsible for the disturbance of grain alignment and hence the relatively high  $\Delta\theta_R$  seen in these two regions where two components of  $\theta_R$  ( $<196^\circ$  and  $\geq 196^\circ$ ) are present. The symmetry axis of the cavity, believed to be carved out by the outflow from HD 200775 (Fuente et al. 1998), is found to be in a direction almost perpendicular to the magnetic field direction. The cavity located to the northwest of HD 200775 is found to be more extended suggesting that this part is relatively more affected by the star than the southeastern cavity. Presence of high-velocity gas in sector 6 supports this observation. In sector 5 also, the presence of additional velocity components disturbs the surrounding material, which results in a higher dispersion in  $\theta_R$ . The additional velocity component is considered to originate from a loop structure close to L1172 (will be discussed in detail in Sharma et al., in prep.). The  $\Delta V$  values estimated for the lines in all sectors are listed in Table 4.

From Fig. 3, it is evident that a majority of the average  $^{12}CO$  ( $J = 1-0$ ) line profiles seem to have multiple velocity components, though we selected the outer envelope of the cloud complex (where we carried out the  $R$ -band polarimetric study), which is of relatively low density. This arises a possibility of overestimation of  $^{12}CO$  linewidth. It would have been better to use  $^{13}CO$ , which was not available in our study. Though we had  $C^{18}O$  data toward this region, but being a high-density gas tracer, we could get emission only in the inner region of the cloud complex, where polarimetric measurements are not available. Therefore, we restrained the linewidth measurements using  $^{12}CO$  only.

#### 4.2. Magnetic field strength in L1172/1174

The strength of the plane-of-sky component of the magnetic field was estimated using the modified Chandrasekhar-Fermi (CF)



relation (Chandrasekhar & Fermi 1953; Ostriker et al. 2001),

$$B_{\text{POS}} = 9.3 \left[ \frac{n_{\text{H}_2}}{\text{cm}^{-3}} \right]^{1/2} \left[ \frac{\Delta V}{\text{kms}^{-1}} \right] \left[ \frac{\Delta\theta}{1^\circ} \right]^{-1} \mu\text{G}, \quad (4)$$

where  $n_{\text{H}_2}$  represents the volume density of hydrogen gas in molecular clouds,  $\Delta V$  is the FWHM obtained from the velocity dispersion  $\sigma V$  ( $\sqrt{8\ln 2} \sigma V$ ), and  $\Delta\theta$  is the dispersion in the position angles. The CF method is applicable for  $\Delta\theta < 25^\circ$ . This method suggests that the strength can be estimated by the analysis of small-scale randomness in the magnetic field lines. The line-of-sight velocity dispersion causes an irregular scatter in the polarization position angles under the assumptions that there is a mean field component in the area of interest, that the turbulence responsible for the magnetic field perturbations is isotropic, and that there is equipartition between the turbulent kinetic and magnetic energy (Heitsch et al. 2001). The CF method of estimating  $B_{\text{POS}}$  is a statistical method that may be in error by a factor of  $\sim 2$  for individual clouds.

The observed  $\Delta\theta_{\text{R,obs}}$  is the joint contribution of both the intrinsic dispersion ( $\Delta\theta_{\text{R}}$ ) and measurement uncertainties ( $\sigma_{\theta_{\text{R}}}$ ) (Lai et al. 2001). Therefore, we obtained the  $\Delta\theta_{\text{R}}$  using  $\Delta\theta_{\text{R}} = \sqrt{(\Delta\theta_{\text{R,obs}}^2 - \sigma_{\theta_{\text{R}}}^2)}$ . The  $\sigma_{\theta_{\text{R}}}$  is the average uncertainty, which was estimated using  $\sigma_{\theta_{\text{R}}} = \sum \sigma_{\theta_{\text{R}_i}} / N$ , where  $\sigma_{\theta_{\text{R}_i}}$  is the measured uncertainty of the  $i^{\text{th}}$  star's polarization angle and  $N$  is the total number of stars. The values of  $\Delta V$  for sectors 1–8 and for the tail, as identified in Fig. 2a, are obtained by fitting Gaussian profiles (single component) to the average  $^{12}\text{CO}$  spectrum generated for the individual regions. The estimated values of  $\Delta V$  are given in the Col. 5 of Table 4.  $\Delta V$  is the combination of both thermal ( $\Delta V_{\text{th}}$ ) and nonthermal ( $\Delta V_{\text{NT}}$ ) gas components along the line-of-sight ( $\Delta V = \sqrt{\Delta V_{\text{th}}^2 + \Delta V_{\text{NT}}^2}$ ) (Myers 1983).  $\Delta V_{\text{th}}$  can be estimated from  $\sigma_{\text{th}} = \sqrt{kT/m}$ , where  $\sigma_{\text{th}}$  is the thermal velocity dispersion of the gas,  $k$  is the Boltzmann constant,  $T$  is the kinetic temperature and  $m$  is molecular weight of the gas.  $T = 10$  K was assumed to estimate the  $\Delta V_{\text{th}}$  in our analysis. We removed the thermal component from the observed linewidth in each sector. The angular extent of the head within the  $9 \times 10^{20} \text{ cm}^{-2}$  contour is  $\sim 0.6^\circ$ , which is  $\sim 3.5$  pc considering its distance as  $\sim 335$  pc (Saha et al. 2020). For the tail, based on the same contour level, the angular extent was found to be  $0.5^\circ$ , which translates to  $\sim 2.9$  pc at 335 pc. Assuming a similar line-of-sight extent for the cloud and using the hydrogen column density values obtained toward individual stars for which we made  $R$ -band polarization measurements, we calculated an average value for  $n_{\text{H}_2}$  for each sectors and the tail region. The  $n_{\text{H}_2}$  thus obtained are given in Col. 6 of Table 4. The uncertainty in the measurement of  $n_{\text{H}_2}$  is taken as 40% of the value (Pokhrel et al. 2016). The  $B_{\text{POS}}$  strength calculated for the head and the tail regions are given in Col. 7 of Table 4. The magnetic field strength is found to be weakest in sector 6, which is due to the combined effect of narrow  $\Delta V$  and relatively high value of  $\Delta\theta_{\text{R}}$ . The average value of magnetic field strength for the entire cloud is found to be  $\sim 30 \mu\text{G}$ .

#### 4.3. Large-scale magnetic field and bulk motion

Overall, the  $B_{\text{POS}}$  geometry in L1172/1174 cloud complex inferred from both the  $R$  band and *Planck* displays an ‘‘S’’ shape morphology with the field lines changing their orientations smoothly as we move from the head to the tail region with  $B_{\text{POS}}$  oriented almost parallel to the main filament of the cloud as

traced by the  $15 \times 10^{20} \text{ cm}^{-2}$  contour as seen in Fig. 1a. In Fig. 4a we show the magnetic field geometry of the region surrounding L1172/1174 and L1147/1158 ( $1.4^\circ \times 1.4^\circ$ ) cloud complexes. The large-scale survey carried out in  $^{13}\text{CO}$  ( $J = 1-0$ ) line of the Cepheus and Cassiopeia regions by Yonekura et al. (1997) suggests that both the complexes share similar radial velocities ( $2.7-2.9 \text{ km s}^{-1}$ ) implying that the two regions are both spatially and kinematically connected. The distance of  $340 \pm 3$  pc to L1147/1158 estimated using the *Gaia* DR2 parallax and the proper motion measurements of the YSOs associated with the complex (Sharma et al. 2020) suggests that both L1147/1158 and L1172/1174 are roughly at similar distance from us. At this distance, the spatial separation between the two complexes is  $\sim 9$  pc.

In Fig. 4b we plot  $P_{\text{p}}$  versus  $\theta_{\text{p}}$  from four regions (square boxes of size  $0.8^\circ \times 0.8^\circ$ ) selected around L1172/1174 cloud complex as shown in Fig. 4a to examine the large-scale magnetic field orientation in the surrounding medium and how it is related to the cloud field lines. The broken lines identify the median values of the two position angle components identified from  $\theta_{\text{R}}$  toward the head and the median value of the  $\theta_{\text{R}}$  toward the tail as shown in Fig. 2b. The median and MAD values of  $\theta_{\text{p}}$  toward L1147/1158 are  $182^\circ$  and  $4^\circ$ , respectively. This is comparable to the  $179^\circ$  component of  $\theta_{\text{R}}$  in the northwestern part of the head region of L1172/1174. The  $\theta_{\text{p}}$  distribution found toward the regions 1, 2, and 3 resembles the  $\theta_{\text{p}}$  distribution found over the whole cloud complex L1172/1174. This is true for both the  $R$  band and the *Planck* polarization results suggesting that the cloud is permeated with the ICM magnetic field. The  $R$ -band polarization seems to be consistent with the ICM large-scale magnetic field (derived from *Planck*) but shows substructures as it follows closely the column density contours (see Fig. 1a). The median values of  $\theta_{\text{p}}$  for regions 1–4 are  $193^\circ \pm 14$ ,  $191^\circ \pm 5$ ,  $175^\circ \pm 6$ , and  $135^\circ \pm 7$ , respectively. The  $\theta_{\text{p}}$  in regions 1 and 2 are consistent with the median value of  $\theta_{\text{R}}$  obtained for the tail region. The median value of  $175^\circ$  obtained for the region 3 is consistent with the  $179^\circ$  component obtained toward sectors 7 and 8 in the head region suggesting that the magnetic field in the head inferred from the  $R$ -band polarization measurements is smoothly joining with the ICM field lines inferred from the *Planck* polarization measurements. The  $135^\circ$  component obtained for the region 4 resembles the change in the magnetic field geometry seen toward the tail part in  $R$ -band polarization measurements again suggesting a smooth merger between the cloud and ICM field lines. The  $\theta_{\text{p}}$  is found to be relatively scattered in region 1 and in its northeastern part, the alignment of  $\theta_{\text{p}}$  is similar to  $\theta_{\text{R}}$  of sectors 2 and 3. Globally, regions in the northwest (L1147/1158, L1172/1174, 2, and 3) show  $\theta_{\text{p}} \sim 180^\circ$  whereas in the southeastern part (including 1 and 4)  $\theta_{\text{p}}$  is highly disturbed.

Based on the Histogram of Relative Orientations analysis (HRO; Soler et al. 2013) with decaying supersonic turbulence, it was shown that in the high-magnetization scenario, the magnetic field changes direction from being parallel to perpendicular with respect to the density structures. The relative orientation becomes random or parallel in the intermediate- or low-magnetization scenario suggesting that the strength of magnetic field may also play a crucial role. The relative orientation is also found to change progressively with increasing column density, from mostly parallel or having no preferred orientation to mostly perpendicular (Planck Collaboration Int. XXXV 2016). Applying HRO analysis, Soler (2019) presented the orientation of  $B_{\text{POS}}$  for the Cepheus flare region using the *Planck* polarization data (Fig. 3; Soler 2019). It was noted that the elongated structure of the cloud complex and  $B_{\text{POS}}$  are almost parallel across all the

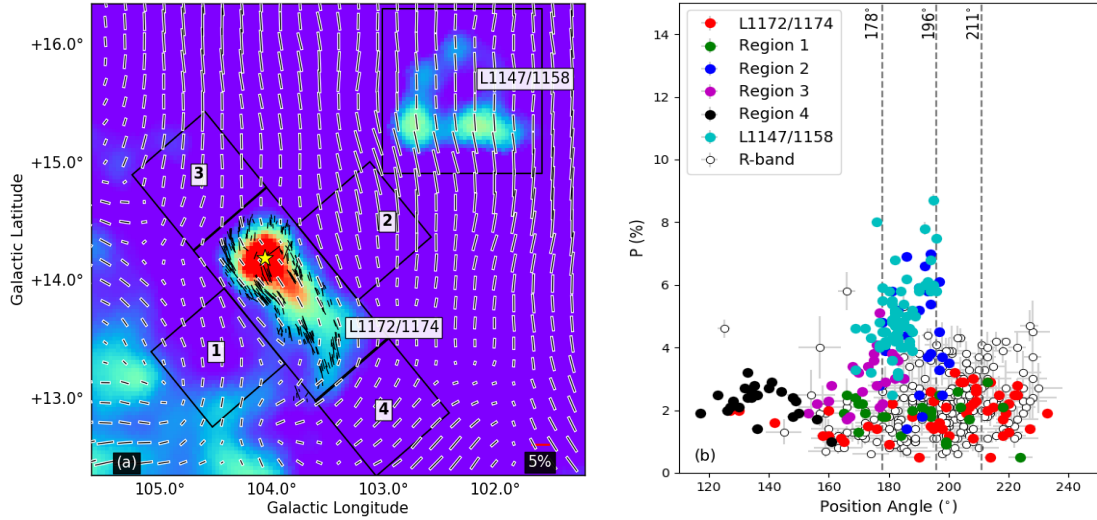


**Fig. 4.** Variation in the projected magnetic field geometry toward L1172/1174 shown in a wider ( $4^\circ \times 4^\circ$ ) area. (a) Magnetic field map (lines in black with white border) of the region covering L1147/1158 and L1172/1174 inferred from the *Planck* polarization measurements. The magnetic field map of L1172/1174 produced using our *R*-band polarization measurements are also shown using black lines. (b) Regions from which we obtained *Planck* polarization measurements shown as boxes (1–4, L1172/1174, and L1147/1158), plotted along with our *R*-band polarization measurements in L1172/1174.

column density values in L1172/1174 cloud complex while they are perpendicular in the L1147/1158 cloud complex, which is clearly visible in Fig. 4a. There is also a marked difference between the magnetic field orientation to the northwestern and southeastern parts of L1172/1174. While the magnetic fields show an almost uni-directional pattern (mostly along  $180^\circ$ ) in the northwestern parts of L1172/1174 where L1147/1158 is also located, to the southeastern parts, the magnetic field lines show more twists and turns.

Studies conducted to investigate the relative orientation between the filamentary structure and the magnetic field in a sample of molecular clouds associated with the Gould Belt report a bimodal distribution of the angles between filaments and magnetic fields with the offsets being either parallel or perpendicular (Li et al. 2013; Gu & Li 2019). Results from simulations (Seifried & Walch 2015) and observational studies (Li et al. 2017) suggest that the bimodality may have implications in cloud’s evolution and subsequent star formation process. The molecular clouds with the long axes perpendicular to the magnetic field directions are shown to have more evenly distributed linear mass across the field lines (Law et al. 2019). Also, these clouds consistently show a lower star formation rate (SFR)/mass for clouds (Li et al. 2017). The perpendicular alignment of magnetic field lines possesses a significantly higher flux compared to the parallel orientation and thus provides a stronger support to the molecular clouds against self-gravity (Li et al. 2017). A total of twelve molecular clouds with their SFR/mass and relative orientations of their long axes with magnetic field lines are listed by Li et al. (2017), based on optical and *Planck* measurements. Of these twelve clouds, six have projected magnetic field aligned perpendicular to the longer axes, while this alignment is parallel for other six clouds. Li et al. (2017) found significant difference in SFR/cloud mass in these two sets of orientations (see Table 5). Our study makes further addition to the findings by Li et al. (2017).

We estimated the SFR in L1172/1174 complex using the total number of YSOs identified toward the cloud and by assuming a mean YSO mass of  $0.5 \pm 0.1 M_\odot$  and age of  $2 \pm 1$  Myr (Evans et al. 2009, 2014; Heiderman et al. 2010; Li et al. 2017). A total of 74 YSOs have been identified so far toward L1172/1174

**Table 5.** SFR per unit cloud mass values (%) of molecular clouds from Li et al. (2017) and from our study.

Cloud name	SFR per unit cloud mass <sup>(†)</sup>	SFR per unit cloud mass <sup>(‡)</sup>	SFR per unit cloud mass <sup>(*)</sup>
Perpendicular alignment			
IC 5146	–	$0.380 \pm 0.18$	–
Pipe Nebula	2.81	–	–
Orion	4.17	–	–
Chamaeleon	–	$1.03 \pm 0.48$	–
Taurus	4.76	0.140	–
Lupus I	4.00	$0.630 \pm 0.52$	–
L1147/1158 <sup>(*)</sup>	–	–	$0.4 \pm 0.3$
Parallel alignment			
Lupus II–VI	6.97	$1.85 \pm 0.74$	–
Corona Australis	9.69	$3.66 \pm 2.4$	–
Cepheus	–	$1.13 \pm 0.62$	–
Ophiuchus	6.10	$2.32 \pm 1.8$	–
Aquila	–	$1.48 \pm 0.8$	–
Perseus	7.98	$1.46 \pm 1.1$	–
L1172/1174 <sup>(*)</sup>	–	–	$2.0 \pm 1.3$

**References.** <sup>(†)</sup>Obtained from Lada et al. (2010). <sup>(‡)</sup>Obtained from Heiderman et al. (2010). <sup>(\*)</sup>Obtained from this work.

complex (Saha et al. 2020). Based on their positions on the color-magnitude diagram produced using the data from the *Gaia* DR2, Saha et al. (2020) found an age of  $\sim 1$ – $2$  Myr for the YSOs, which is consistent with the median age of  $\sim 1.6$  Myr determined by Kun et al. (2009), and thus, in turn, similar to the age we assumed for the estimation of SFR in this cloud complex. Also, the majority of the sources identified so far in L1172/1174 complex are of low-mass M types ( $0.1$ – $0.7 M_\odot$ ), which is found to be consistent with our assumptions. The SFR thus calculated is found to be  $19 \pm 10 M_\odot \text{ Myr}^{-1}$ . The mass of the cloud was estimated by summing up all those pixels having the hydrogen column density threshold of  $9 \times 10^{20} \text{ cm}^{-2}$  ( $A_V \gtrsim 1.0$  magnitude) and using it in the expression  $M = N(\text{H}_2)m_{\text{H}}\mu A$  (Bresnahan et al. 2018), where  $M$  is the cloud mass per pixel,

$N(\text{H}_2)$  indicates the  $\text{H}_2$  column density,  $m_{\text{H}}$  represents mass of a hydrogen atom,  $\mu = 2.86$ , the mean particle mass (assuming  $\sim 70\%$   $\text{H}_2$  by mass), and  $A$  represents the area of each pixel. We estimated the area  $A$  using  $(\pi/180/3600)^2 D(\text{cm})^2 R''^2$ , where  $D$  is the distance to the cloud complex and  $R''$  is the size of one pixel. We estimated a cloud mass of  $950 \pm 380 M_{\odot}$ . The error is estimated by propagating the uncertainties in the column density estimation and in the distance. Recently, Di Francesco et al. (2020) estimated the mass of L1172/1174 as  $1000 M_{\odot}$  with  $A_V > 1$ , which is consistent with the mass we obtained. Thus the SFR/mass estimated for L1172/1174 is  $2.0 \pm 1.3\% \text{ Myr}^{-1}$ , which is comparable with the mean value  $1.98 \pm 0.92\% \text{ Myr}^{-1}$  obtained by Li et al. (2017), for the clouds with parallel alignments (e.g., Ophiuchus, Corona Australis, Aquila, Perseus etc.). Similarly, we estimated the SFR/mass of the neighboring cloud complex L1147/1158, which has its long axis almost perpendicular to the projected magnetic field direction. Considering the same hydrogen column density threshold ( $9 \times 10^{20} \text{ cm}^{-2}$ ) condition, the mass of L1147/1158 is estimated to be  $800 \pm 320 M_{\odot}$ , which is consistent with the mass  $790 M_{\odot}$ , obtained by Di Francesco et al. (2020). A total of 14 YSO candidates (Kirk et al. 2009) including PV Cep are distributed within the defined threshold. The SFR is computed as  $3.5 \pm 1.9 M_{\odot} \text{ Myr}^{-1}$ . Therefore, the estimated SFR/mass for L1147/1158 is  $0.4 \pm 0.3\% \text{ Myr}^{-1}$ , which is significantly lower than the same obtained for L1172/1174. But it is consistent with the mean value for the clouds having magnetic field lines perpendicular to their long axes ( $0.620 \pm 0.37\% \text{ Myr}^{-1}$ ; Li et al. 2017). These results further support the claim by Li et al. (2017) that if the magnetic field lines are aligned parallel to the cloud's long axis (like in L1172/1174, Ophiuchus, Aquila, Perseus etc.), the SFR is found to be higher than in the clouds where the magnetic field lines are aligned perpendicular to the cloud's long axis (like in L1147/1158, IC 5146, Pipe Nebula, Taurus etc.).

## 5. Summary and conclusion

We present the results of our  $R$ -band polarization measurements of 249 sources projected on the cloud complex L1172/1174. Combining our results with those from the *Planck* polarization measurements of the region containing the complex, we studied the magnetic field geometry of the cloud and its relationship with the ICM magnetic field. We summarize the results obtained from this work below:

- The magnetic field geometry inferred from our  $R$ -band polarization measurements and from *Planck* are found to be in good agreement throughout the cloud. The magnetic field is found to be smooth (not chaotic) and oriented along the hub-filament structure of the cloud. The only changes noticed are toward the extreme ends of the head and the tail regions where the magnetic field lines are found to join smoothly with the ambient magnetic fields in the ICM.
- Overall, there is not much effect of the presence of HD 200775 on the magnetic field geometry of the surrounding region except toward the northwestern part of HD 200775 where field lines are showing a relatively large dispersion in the magnetic field vectors. The  $^{12}\text{CO}$  line profile shows a presence of high-velocity clouds in this region, which may be responsible for disturbing the magnetic field geometry.
- The mean magnetic field strength for the entire cloud was found to be  $\sim 30 \mu\text{G}$ . Globally, the magnetic field geometry inferred from the *Planck* polarization is found to be oriented along a mean position angle of  $180^\circ$  toward the northwestern side of L1172/1174 where the cloud complex L1147/1158

is located. At the location of the cloud, the magnetic field lines change to a mean position angle of  $200^\circ$  and then to the southeastern side of L1172/1174, the magnetic field lines show more twists and turns.

- The higher SFR/mass of  $2.0 \pm 1.3\% \text{ Myr}^{-1}$  found for L1172/1174, compared to  $0.4 \pm 0.3\% \text{ Myr}^{-1}$  for L1147/1158, is consistent with the earlier results, which suggests that the molecular clouds with magnetic field lines oriented parallel to the cloud elongation are found to show relatively high values of SFR compared to those with field lines perpendicular to the cloud elongation.

As a whole, this study helps us to understand the morphology of the projected magnetic field geometry toward the inner high-density as well as the outer low-density regions of the L1172/1174 cloud complex and also its impact in the SFR.

*Acknowledgements.* We thank Dr. Archana Soam and Neha Sharma, and all the supporting staff at ARIES, Nainital who made these observations possible. C.W.L. was supported by the Basic Science Research Program (2019R1A2C1010851) through the National Research Foundation of Korea. T.G. acknowledges support from the Science and Engineering Research Board of the Department of Science and Technology, Govt. of India, grant number SERB/ECR/2018/000826. This work has made use of data from the following sources: (1) the *Planck* Legacy Archive (PLA) contains all public products originating from the *Planck* mission, and we take the opportunity to thank ESA/*Planck* and the *Planck* collaboration for the same. (2) European Space Agency (ESA) mission *Gaia* (<https://www.cosmos.esa.int/gaia>), processed by the *Gaia* Data Processing and Analysis Consortium (DPAC, <https://www.cosmos.esa.int/web/gaia/dpac/consortium>). Funding for the DPAC has been provided by national institutions, in particular the institutions participating in the *Gaia* Multilateral Agreement. This research also has made use of the SIMBAD database, operated at CDS, Strasbourg, France.

## References

- Alina, D., Ristorcelli, I., Montier, L., et al. 2019, *MNRAS*, **485**, 2825  
 Alves, F. O., Franco, G. A. P., & Girart, J. M. 2008, *A&A*, **486**, L13  
 André, R., & Kremer, G. M. 2014, ArXiv e-prints [arXiv:1411.6096]  
 André, P., Men'shchikov, A., Bontemps, S., et al. 2010, *A&A*, **518**, L102  
 Arzoumanian, D., André, P., Didelon, P., et al. 2011, *A&A*, **529**, L6  
 Bailer-Jones, C. A. L. 2015, *PASP*, **127**, 994  
 Bailer-Jones, C. A. L., Rybizki, J., Fouesneau, M., Mantelet, G., & Andrae, R. 2018, *AJ*, **156**, 58  
 Ballesteros-Paredes, J., Klessen, R. S., Mac Low, M. M., & Vazquez-Semadeni, E. 2007, *Protostars and Planets V*, eds. B. Reipurth, D. Jewitt, & K. Keil (Tucson: University of Arizona Press), 63  
 Banerjee, R., Vázquez-Semadeni, E., Hennebelle, P., & Klessen, R. S. 2009, *MNRAS*, **398**, 1082  
 Bastien, P. 1982, *A&AS*, **48**, 153  
 Bastien, P. 1985, *ApJS*, **59**, 277  
 Bastien, P., & Landstreet, J. D. 1979, *ApJ*, **229**, L137  
 Beattie, J. R., & Federrath, C. 2020, *MNRAS*, **492**, 668  
 Bhatt, H. C., & Jain, S. K. 1992, *MNRAS*, **257**, 57  
 Bohlin, R. C., Savage, B. D., & Drake, J. F. 1978, *ApJ*, **224**, 132  
 Bresnahan, D., Ward-Thompson, D., Kirk, J. M., et al. 2018, *A&A*, **615**, A125  
 Chandrasekhar, S., & Fermi, E. 1953, *ApJ*, **118**, 113  
 Chapman, N. L., Goldsmith, P. F., Pineda, J. L., et al. 2011, *ApJ*, **741**, 21  
 Chen, C.-Y., & Ostriker, E. C. 2014, *ApJ*, **785**, 69  
 Chen, H.-R. V., Zhang, Q., Wright, M. C. H., et al. 2019, *ApJ*, **875**, 24  
 Davis, Jr. L., & Greenstein, J. L. 1951, *ApJ*, **114**, 206  
 Di Francesco, J., Keown, J., Fallscheer, C., et al. 2020, *ApJ*, **904**, 172  
 Dolginov, A. Z., & Mitrofanov, I. G. 1976, *Ap&SS*, **43**, 291  
 Draine, B. T., & Weingartner, J. C. 1996, *ApJ*, **470**, 551  
 Draine, B. T., & Weingartner, J. C. 1997, *ApJ*, **480**, 633  
 Dutta, S., Mondal, S., Samal, M. R., & Jose, J. 2018, *ApJ*, **864**, 154  
 Elsasser, H., & Staude, H. J. 1978, *A&A*, **70**, L3  
 Eswaraiyah, C., Pandey, A. K., Maheswar, G., et al. 2011, *MNRAS*, **411**, 1418  
 Eswaraiyah, C., Pandey, A. K., Maheswar, G., et al. 2012, *MNRAS*, **419**, 2587  
 Eswaraiyah, C., Lai, S.-P., Chen, W.-P., et al. 2017, *ApJ*, **850**, 195  
 Evans, Neal J., I., Dunham, M. M., Jørgensen, J. K., et al. 2009, *ApJS*, **181**, 321  
 Evans, Neal J., I., Heiderman, A., & Vutisalchavakul, N. 2014, *ApJ*, **782**, 114  
 Fiege, J. D., & Pudritz, R. E. 2000, *MNRAS*, **311**, 105  
 Franco, G. A. P., Alves, F. O., & Girart, J. M. 2010, *ApJ*, **723**, 146



- Fuente, A., Martin-Pintado, J., Rodriguez-Franco, A., & Moriarty-Schieven, G. D. 1998, *A&A*, **339**, 575
- Gaia Collaboration (Brown, A. G. A., et al.) 2018, *A&A*, **616**, A1
- Gold, T. 1952a, *Nature*, **169**, 322
- Gold, T. 1952b, *MNRAS*, **112**, 215
- Gómez, G. C., & Vázquez-Semadeni, E. 2014, *ApJ*, **791**, 124
- Gómez, G. C., Vázquez-Semadeni, E., & Zamora-Avilés, M. 2018, *MNRAS*, **480**, 2939
- Goodman, A. A. 1995, *ASP Conf. Ser.*, **73**
- Goodman, A. A. 1996, *ASP Conf. Ser.*, **97**, 325
- Goodman, A. A., Bastien, P., Menard, F., & Myers, P. C. 1990, *ApJ*, **359**, 363
- Goodman, A. A., Jones, T. J., Lada, E. A., & Myers, P. C. 1992, *ApJ*, **399**, 108
- Goodman, A. A., Jones, T. J., Lada, E. A., & Myers, P. C. 1995, *ApJ*, **448**, 748
- Górski, K. M., Hivon, E., Banday, A. J., et al. 2005, *ApJ*, **622**, 759
- Greaves, J. S., Holland, W. S., Minchin, N. R., Murray, A. G., & Stevens, J. A. 1999, *A&A*, **344**, 668
- Gu, Q., & Li, H.-b. 2019, *ApJ*, **871**, L15
- Guetter, H. H., & Vrba, F. J. 1989, *AJ*, **98**, 611
- Hajigholi, M., Persson, C. M., Wirstrom, E. S., et al. 2016, *A&A*, **585**, A158
- Hall, J. S. 1949, *Science*, **109**, 166
- Hamaker, J. P., & Bregman, J. D. 1996, *A&AS*, **117**, 161
- Harjunpää, P., Kaas, A. A., Carlqvist, P., & Gahm, G. F. 1999, *A&A*, **349**, 912
- Hartmann, L., Ballesteros-Paredes, J., & Bergin, E. A. 2001, *ApJ*, **562**, 852
- Heiderman, A., Evans, Neal J. I., Allen, L. E., et al. 2010, *ApJ*, **723**, 1019
- Heiles, C. 2000, *AJ*, **119**, 923
- Heitsch, F., Zweibel, E. G., Mac Low, M.-M., Li, P., & Norman, M. L. 2001, *ApJ*, **561**, 800
- Hennebelle, P. 2013, *A&A*, **556**, A153
- Heyer, M., Goldsmith, P. F., Yıldız, U. A., et al. 2016, *MNRAS*, **461**, 3918
- Hildebrand, R. H., Dragovan, M., & Novak, G. 1984, *ApJ*, **284**, L51
- Hill, T., Motte, F., Didelon, P., et al. 2011, *A&A*, **533**, A94
- Hiltner, W. A. 1949, *ApJ*, **109**, 471
- Iffrig, O., & Hennebelle, P. 2017, *A&A*, **604**, A70
- Inutsuka, S.-i., Inoue, T., Iwasaki, K., & Hosokawa, T. 2015, *A&A*, **580**, A49
- Jiménez-Serra, I., Caselli, P., Fontani, F., et al. 2014, *MNRAS*, **439**, 1996
- Jeong, I.-G., Kang, H., Jung, J., et al. 2019, *J. Korean Astron. Soc.*, **52**, 227
- Kirk, J. M., Ward-Thompson, D., Di Francesco, J., et al. 2009, *ApJS*, **185**, 198
- Kirk, H., Myers, P. C., Bourke, T. L., et al. 2013, *ApJ*, **766**, 115
- Kirk, H., Klassen, M., Pudritz, R., & Pillsworth, S. 2015, *ApJ*, **802**, 75
- Klessen, R. S., Heitsch, F., & Mac Low, M.-M. 2000, *ApJ*, **535**, 887
- Koch, P. M., Tang, Y.-W., & Ho, P. T. P. 2013, *ApJ*, **775**, 77
- Koch, P. M., Tang, Y.-W., Ho, P. T. P., et al. 2014, *ApJ*, **797**, 99
- Kun, M., Balog, Z., Kenyon, S. J., Mamajek, E. E., & Gutermuth, R. A. 2009, *ApJS*, **185**, 451
- Lada, C. J., Lombardi, M., & Alves, J. F. 2010, *ApJ*, **724**, 687
- Lai, S.-P., Crutcher, R. M., Girart, J. M., & Rao, R. 2001, *ApJ*, **561**, 864
- Law, C. Y., Li, H. B., & Leung, P. K. 2019, *MNRAS*, **484**, 3604
- Lazarian, A., & Hoang, T. 2007, *MNRAS*, **378**, 910
- Lee, H. M., & Draine, B. T. 1985, *ApJ*, **290**, 211
- Li, H.-b., Dowell, C. D., Goodman, A., Hildebrand, R., & Novak, G. 2009, *ApJ*, **704**, 891
- Li, H.-B., Blundell, R., Hedden, A., et al. 2011, *MNRAS*, **411**, 2067
- Li, H.-b., Fang, M., Henning, T., & Kainulainen, J. 2013, *MNRAS*, **436**, 3707
- Li, H. B., Goodman, A., Sridharan, T. K., et al. 2014, in *Protostars and Planets VI*, eds. H. Beuther, R. S. Klessen, C. P. Dullemond, & T. Henning (Tucson: University of Arizona Press), 101
- Li, H.-B., Jiang, H., Fan, X., Gu, Q., & Zhang, Y. 2017, *Nat. Astron.*, **1**, 0158
- Lu, X., Zhang, Q., Liu, H. B., et al. 2018, *ApJ*, **855**, 9
- Luri, X., Brown, A. G. A., Sarro, L. M., et al. 2018, *A&A*, **616**, A9
- Lynds, B. T. 1962, *ApJS*, **7**, 1
- Manoj, P., Bhatt, H. C., Maheswar, G., & Muneer, S. 2006, *ApJ*, **653**, 657
- Matthaeus, W. H., Pouquet, A., Mininni, P. D., Dmitruk, P., & Breech, B. 2008, *Phys. Rev. Lett.*, **100**, 085003
- Matthews, B. C., McPhee, C. A., Fissel, L. M., & Curran, R. L. 2009, *ApJS*, **182**, 143
- Medhi, B. J., Maheswar, G., Pandey, J. C., Kumar, T. S., & Sagar, R. 2008, *MNRAS*, **388**, 105
- Ménard, F. C. 2005, *ASP Conf. Ser.*, **343**, 128
- Molina, F. Z., Glover, S. C. O., Federrath, C., & Klessen, R. S. 2012, *MNRAS*, **423**, 2680
- Molinari, S., Swinyard, B., Bally, J., et al. 2010, *A&A*, **518**, L100
- Montier, L., Plaszczyński, S., Levrier, F., et al. 2015, *A&A*, **574**, A135
- Myers, P. C. 1983, *ApJ*, **270**, 105
- Myers, P. C. 2009, *ApJ*, **700**, 1609
- Nagai, T., Inutsuka, S.-i., & Miyama, S. M. 1998, *ApJ*, **506**, 306
- Nakamura, F., & Li, Z.-Y. 2008, *ApJ*, **687**, 354
- Neha, S., Maheswar, G., Soam, A., Lee, C. W., & Tej, A. 2016, *A&A*, **588**, A45
- Neha, S., Maheswar, G., Soam, A., & Lee, C. W. 2018, *MNRAS*, **476**, 4442
- Ostriker, E. C., Stone, J. M., & Gammie, C. F. 2001, *ApJ*, **546**, 980
- Padoan, P., & Nordlund, Å. 2002, *ApJ*, **576**, 870
- Padoan, P., Juvela, M., Goodman, A. A., & Nordlund, Å. 2001, *ApJ*, **553**, 227
- Palmeirim, P., André, P., Kirk, J., et al. 2013, *A&A*, **550**, A38
- Peretto, N., Fuller, G. A., André, P., et al. 2014, *A&A*, **561**, A83
- Pilbratt, G. L., Riedinger, J. R., Passvogel, T., et al. 2010, *A&A*, **518**, L1
- Pillai, T. G. S., Clemens, D. P., Reissl, S., et al. 2020, *Nat. Astron.*, **4**, 1195
- Planck Collaboration I. 2014, *A&A*, **571**, A1
- Planck Collaboration I. 2016, *A&A*, **594**, A1
- Planck Collaboration Int. XIX. 2015, *A&A*, **576**, A104
- Planck Collaboration Int. XXX. 2016, *A&A*, **586**, A133
- Planck Collaboration Int. XXXV. 2016, *A&A*, **586**, A138
- Pokhrel, R., Gutermuth, R., Ali, B., et al. 2016, *MNRAS*, **461**, 22
- Qiu, K., Zhang, Q., Menten, K. M., et al. 2014, *ApJ*, **794**, L18
- Ramaprakash, A. N., Gupta, R., Sen, A. K., & Tandon, S. N. 1998, *A&AS*, **128**, 369
- Rautela, B. S., Joshi, G. C., & Pandey, J. C. 2004, *Bull. Astron. Soc. India*, **32**, 159
- Rayner, T. S. M., Griffin, M. J., Schneider, N., et al. 2017, *A&A*, **607**, A22
- Rector, T. A., & Schweiker, H. 2013, *AJ*, **145**, 35
- Saha, P., Gopinathan, M., Kamath, U., et al. 2020, *MNRAS*, **494**, 5851
- Sato, S. 1988, *Prog. Theor. Phys. Suppl.*, **96**, 37
- Sato, S., Tamura, M., Nagata, T., et al. 1988, *MNRAS*, **230**, 321
- Schmidt, G. D., Elston, R., & Lupie, O. L. 1992, *AJ*, **104**, 1563
- Schneider, N., Csengeri, T., Bontemps, S., et al. 2010, *A&A*, **520**, A49
- Seifrid, D., & Walch, S. 2015, *MNRAS*, **452**, 2410
- Sharma, E., Gopinathan, M., Soam, A., et al. 2020, *A&A*, **639**, A133
- Shetty, R., & Ostriker, E. C. 2006, *ApJ*, **647**, 997
- Shimajiri, Y., André, P., Palmeirim, P., et al. 2019, *A&A*, **623**, A16
- Soam, A., Maheswar, G., Bhatt, H. C., Lee, C. W., & Ramaprakash, A. N. 2013, *MNRAS*, **432**, 1502
- Soam, A., Maheswar, G., & Eswaraiiah, C. 2014, *Ap&SS*, **350**, 251
- Soam, A., Kwon, J., Maheswar, G., Tamura, M., & Lee, C. W. 2015a, *ApJ*, **803**, L20
- Soam, A., Maheswar, G., Lee, C. W., et al. 2015b, *A&A*, **573**, A34
- Soam, A., Maheswar, G., Lee, C. W., Neha, S., & Andersson, B.-G. 2017, *MNRAS*, **465**, 559
- Soam, A., Maheswar, G., Lee, C. W., Neha, S., & Kim, K.-T. 2018a, *MNRAS*, **476**, 4782
- Soam, A., Pattle, K., Ward-Thompson, D., et al. 2018b, *ApJ*, **861**, 65
- Soam, A., Lee, C. W., Andersson, B. G., et al. 2019, *ApJ*, **883**, 9
- Soler, J. D. 2019, *A&A*, **629**, A96
- Soler, J. D., & Hennebelle, P. 2017, *A&A*, **607**, A2
- Soler, J. D., Hennebelle, P., Martin, P. G., et al. 2013, *ApJ*, **774**, 128
- Soler, J. D., Alves, F., Boulanger, F., et al. 2016, *A&A*, **596**, A93
- Stone, J. M., Ostriker, E. C., & Gammie, C. F. 1998, *ApJ*, **508**, L99
- Strom, S. E. 1977, *IAU Symp.*, **75**, 179
- Sugitani, K., Nakamura, F., Tamura, M., et al. 2010, *ApJ*, **716**, 299
- Sugitani, K., Nakamura, F., Watanabe, M., et al. 2011, *ApJ*, **734**, 63
- Tachihara, K., Onishi, T., Mizuno, A., & Fukui, Y. 2002, *A&A*, **385**, 909
- Tamura, M., Hashimoto, J., Kandori, R., et al. 2011, *ASP Conf. Ser.*, **449**, 207
- Tazaki, R., Lazarian, A., & Nomura, H. 2017, *ApJ*, **839**, 56
- The, P. S., de Winter, D., & Perez, M. R. 1994, *A&AS*, **104**, 315
- Treviño-Morales, S. P., Fuente, A., Sánchez-Monge, Á., et al. 2019, *A&A*, **629**, A81
- Tritsis, A., & Tassis, K. 2016, *MNRAS*, **462**, 3602
- Van Loo, S., Keto, E., & Zhang, Q. 2014, *ApJ*, **789**, 37
- Vink, J. S., Drew, J. E., Harries, T. J., Oudmajer, R. D., & Unruh, Y. 2005, *MNRAS*, **359**, 1049
- Vrba, F. J., Strom, S. E., & Strom, K. M. 1976, *AJ*, **81**, 958
- Wardle, J. F. C., & Kronberg, P. P. 1974, *ApJ*, **194**, 249
- Ward-Thompson, D., Kirk, J. M., Crutcher, R. M., et al. 2000, *ApJ*, **537**, L135
- Ward-Thompson, D., Sen, A. K., Kirk, J. M., & Nutter, D. 2009, *MNRAS*, **398**, 394
- Wareing, C. J., Pittard, J. M., Falle, S. A. E. G., & Van Loo, S. 2016, *MNRAS*, **459**, 1803
- Watt, G. D., Burton, W. B., Choe, S. U., & Liszt, H. S. 1986, *A&A*, **163**, 194
- Weston, E. B. 1953, *AJ*, **58**, 48
- Whittet, D. C. B. 2005, *ASP Conf. Ser.*, **343**, 321
- Williams, G. M., Peretto, N., Avison, A., Duarte-Cabral, A., & Fuller, G. A. 2018, *A&A*, **613**, A11
- Wolf, S., Launhardt, R., & Henning, T. 2003, *ApJ*, **592**, 233
- Yonekura, Y., Dobashi, K., Mizuno, A., Ogawa, H., & Fukui, Y. 1997, *ApJS*, **110**, 21
- Yuan, J.-H., Wu, Y., Li, J. Z., Yu, W., & Miller, M. 2013, *MNRAS*, **429**, 954
- Zamora-Avilés, M., Ballesteros-Paredes, J., & Hartmann, L. W. 2017, *MNRAS*, **472**, 467
- Zonca, A., Singer, L., Lenz, D., et al. 2019, *J. Open Source Softw.*, **4**, 1298

## Appendix A: Table

Table A.1. R-band polarimetric results of 249 stars observed toward L1172/1174.

Star Id	$l$ (°)	$b$ (°)	$P \pm \sigma_P$ (%)	$\theta \pm \sigma_\theta$ (°)	$d \pm \sigma_d$ (pc)	Star Id	$l$ (°)	$b$ (°)	$P \pm \sigma_P$ (%)	$\theta \pm \sigma_\theta$ (°)	$d \pm \sigma_d$ (pc)
1	103.369563	13.535764	1.8 ± 0.4	191 ± 5	1335 <sup>+71</sup> <sub>-64</sub>	52	103.631329	13.531912	3.4 ± 0.6	215 ± 4	778 <sup>+29</sup> <sub>-27</sub>
2	103.376949	13.534869	1.9 ± 0.4	192 ± 4	461 <sup>+4</sup> <sub>-4</sub>	53	103.632864	14.049986	2.5 ± 0.4	196 ± 4	1042 <sup>+28</sup> <sub>-26</sub>
3	103.388335	13.423807	3.6 ± 1.0	194 ± 7	1269 <sup>+78</sup> <sub>-70</sub>	54	103.638274	13.523002	2.3 ± 0.2	205 ± 2	498 <sup>+48</sup> <sub>-40</sub>
4	103.391221	13.371439	2.0 ± 0.1	189 ± 1	1295 <sup>+43</sup> <sub>-40</sub>	55	103.648487	14.041594	1.5 ± 0.3	198 ± 5	1429 <sup>+54</sup> <sub>-50</sub>
5	103.396714	13.370003	0.8 ± 0.3	184 ± 6	882 <sup>+19</sup> <sub>-18</sub>	56	103.653112	13.516389	2.3 ± 0.5	203 ± 5	1841 <sup>+114</sup> <sub>-102</sub>
6	103.399226	13.548511	1.8 ± 0.5	188 ± 6	2088 <sup>+160</sup> <sub>-139</sub>	57	103.657643	13.573459	2.7 ± 0.4	201 ± 4	1874 <sup>+146</sup> <sub>-127</sub>
7	103.403268	13.643440	2.8 ± 0.5	205 ± 5	2619 <sup>+266</sup> <sub>-222</sub>	58	103.662384	13.512556	1.6 ± 0.2	199 ± 3	856 <sup>+11</sup> <sub>-11</sub>
8	103.405470	13.542955	2.3 ± 0.4	188 ± 4	5459 <sup>+1031</sup> <sub>-782</sub>	59	103.662619	13.545521	1.8 ± 0.1	207 ± 2	355 <sup>+2</sup> <sub>-2</sub>
9	103.407969	13.506287	2.1 ± 0.1	193 ± 1	475 <sup>+4</sup> <sub>-4</sub>	60	103.664697	13.001426	0.7 ± 0.2	186 ± 5	741 <sup>+11</sup> <sub>-10</sub>
10	103.413906	13.654661	1.5 ± 0.5	200 ± 7	6033 <sup>+1509</sup> <sub>-1111</sub>	61	103.666569	13.051837	1.3 ± 0.4	145 ± 6	2075 <sup>+177</sup> <sub>-152</sub>
11	103.420810	13.460331	1.9 ± 0.4	200 ± 5	469 <sup>+4</sup> <sub>-4</sub>	62	103.680989	13.501700	1.3 ± 0.1	205 ± 2	1686 <sup>+110</sup> <sub>-98</sub>
12	103.425854	13.408299	2.7 ± 0.9	185 ± 8	3717 <sup>+434</sup> <sub>-355</sub>	63	103.681499	13.550944	2.0 ± 0.3	206 ± 4	1293 <sup>+40</sup> <sub>-38</sub>
13	103.427039	13.500412	2.4 ± 0.1	191 ± 1	659 <sup>+6</sup> <sub>-6</sub>	64	103.682929	13.658846	3.8 ± 0.2	201 ± 1	1709 <sup>+83</sup> <sub>-76</sub>
14	103.432185	13.336416	2.1 ± 0.1	197 ± 1	457 <sup>+5</sup> <sub>-5</sub>	65	103.683858	13.653563	1.7 ± 0.3	204 ± 5	6516 <sup>+1528</sup> <sub>-1141</sub>
15	103.432276	13.357525	2.1 ± 0.1	191 ± 1	552 <sup>+8</sup> <sub>-8</sub>	66	103.685928	13.652803	2.7 ± 0.3	203 ± 2	1847 <sup>+86</sup> <sub>-79</sub>
16	103.433914	13.462983	1.7 ± 0.1	202 ± 1	665 <sup>+10</sup> <sub>-10</sub>	67	103.690315	13.629575	3.5 ± 0.6	206 ± 4	1208 <sup>+32</sup> <sub>-31</sub>
17	103.445397	13.488413	1.8 ± 0.6	180 ± 7	2957 <sup>+205</sup> <sub>-179</sub>	68	103.691753	13.496346	1.1 ± 0.3	195 ± 5	1386 <sup>+50</sup> <sub>-46</sub>
18	103.446267	13.324590	2.4 ± 0.5	193 ± 5	3176 <sup>+226</sup> <sub>-198</sub>	69	103.699510	13.625001	4.0 ± 0.5	223 ± 3	644 <sup>+40</sup> <sub>-36</sub>
19	103.446568	13.834850	1.3 ± 0.4	196 ± 6	3428 <sup>+319</sup> <sub>-271</sub>	70	103.712075	14.044119	1.4 ± 0.2	189 ± 3	4309 <sup>+1100</sup> <sub>-782</sub>
20	103.453856	13.366588	2.5 ± 0.6	191 ± 6	2097 <sup>+240</sup> <sub>-196</sub>	71	103.717844	14.098736	1.0 ± 0.1	189 ± 3	785 <sup>+11</sup> <sub>-11</sub>
21	103.466449	13.297720	1.5 ± 0.3	200 ± 4	779 <sup>+21</sup> <sub>-20</sub>	72	103.718710	13.585106	2.6 ± 0.8	191 ± 7	2087 <sup>+382</sup> <sub>-284</sub>
22	103.469665	13.821971	1.6 ± 0.1	200 ± 2	457 <sup>+3</sup> <sub>-3</sub>	73	103.727308	14.084367	3.7 ± 0.6	185 ± 4	1888 <sup>+371</sup> <sub>-271</sub>
23	103.484429	13.259809	2.2 ± 0.5	200 ± 5	658 <sup>+13</sup> <sub>-13</sub>	74	103.728869	14.078656	2.3 ± 0.5	188 ± 6	722 <sup>+22</sup> <sub>-20</sub>
24	103.496048	13.316274	2.2 ± 0.3	201 ± 3	1892 <sup>+213</sup> <sub>-175</sub>	75	103.730889	14.107847	3.8 ± 0.4	206 ± 3	1903 <sup>+1205</sup> <sub>-641</sub>
25	103.500559	13.963767	0.8 ± 0.3	202 ± 6	1800 <sup>+55</sup> <sub>-52</sub>	76	103.735578	13.086863	0.6 ± 0.1	198 ± 2	388 <sup>+4</sup> <sub>-4</sub>
26	103.513589	13.762300	2.2 ± 0.4	207 ± 5	765 <sup>+14</sup> <sub>-14</sub>	77	103.737300	13.592209	1.9 ± 0.2	194 ± 3	946 <sup>+17</sup> <sub>-16</sub>
27	103.515728	13.971093	1.8 ± 0.2	191 ± 2	6644 <sup>+939</sup> <sub>-753</sub>	78	103.740288	14.046160	3.8 ± 1.0	198 ± 7	3209 <sup>+511</sup> <sub>-395</sub>
28	103.517554	13.306443	2.3 ± 0.5	195 ± 5	3523 <sup>+402</sup> <sub>-330</sub>	79	103.743451	13.589382	2.2 ± 0.6	194 ± 6	5048 <sup>+1172</sup> <sub>-854</sub>
29	103.522295	13.800443	2.0 ± 0.2	192 ± 2	1588 <sup>+89</sup> <sub>-80</sub>	80	103.743481	14.053415	3.2 ± 0.5	200 ± 4	2627 <sup>+683</sup> <sub>-468</sub>
30	103.524179	13.922084	2.2 ± 0.3	188 ± 3	804 <sup>+26</sup> <sub>-24</sub>	81	103.750202	13.621534	1.9 ± 0.4	214 ± 5	1103 <sup>+49</sup> <sub>-45</sub>
31	103.527084	13.154722	1.7 ± 0.2	184 ± 3	879 <sup>+13</sup> <sub>-12</sub>	82	103.751125	13.066935	3.9 ± 0.8	201 ± 5	1918 <sup>+240</sup> <sub>-193</sub>
32	103.528496	13.281828	1.9 ± 0.2	192 ± 3	1014 <sup>+27</sup> <sub>-26</sub>	83	103.751810	14.198525	2.0 ± 0.2	214 ± 3	539 <sup>+7</sup> <sub>-7</sub>
33	103.530729	13.817294	2.2 ± 0.2	199 ± 2	426 <sup>+3</sup> <sub>-3</sub>	84	103.753142	14.055722	3.9 ± 0.4	200 ± 3	689 <sup>+18</sup> <sub>-17</sub>
34	103.531432	13.964377	2.1 ± 0.1	189 ± 1	2415 <sup>+232</sup> <sub>-196</sub>	85	103.753376	14.158306	5.8 ± 0.6	166 ± 3	670 <sup>+29</sup> <sub>-26</sub>
35	103.532947	13.236985	3.5 ± 0.5	190 ± 4	2165 <sup>+250</sup> <sub>-204</sub>	86	103.757171	13.044135	1.1 ± 0.1	186 ± 2	1510 <sup>+62</sup> <sub>-57</sub>
36	103.536011	13.799642	3.1 ± 0.2	204 ± 1	2322 <sup>+161</sup> <sub>-142</sub>	87	103.759157	14.202982	1.9 ± 0.6	195 ± 8	1140 <sup>+47</sup> <sub>-43</sub>
37	103.547924	13.271056	2.2 ± 0.1	198 ± 1	1146 <sup>+34</sup> <sub>-32</sub>	88	103.771324	14.083528	2.3 ± 0.5	216 ± 6	1787 <sup>+179</sup> <sub>-150</sub>
38	103.561086	13.923598	1.3 ± 0.3	207 ± 5	773 <sup>+13</sup> <sub>-12</sub>	89	103.779461	14.166562	1.3 ± 0.4	199 ± 8	3176 <sup>+255</sup> <sub>-221</sub>
39	103.561332	13.119313	1.1 ± 0.3	159 ± 5	1108 <sup>+47</sup> <sub>-43</sub>	90	103.784884	13.017830	1.0 ± 0.2	176 ± 3	2308 <sup>+99</sup> <sub>-92</sub>
40	103.569513	13.423153	1.9 ± 0.1	202 ± 1	751 <sup>+7</sup> <sub>-7</sub>	91	103.786605	14.168643	0.9 ± 0.1	206 ± 2	756 <sup>+16</sup> <sub>-15</sub>
41	103.576086	13.925862	1.8 ± 0.4	195 ± 5	1175 <sup>+32</sup> <sub>-30</sub>	92	103.788275	14.044542	3.0 ± 0.8	213 ± 8	380 <sup>+8</sup> <sub>-7</sub>
42	103.577631	13.424342	1.9 ± 0.6	195 ± 6	4283 <sup>+943</sup> <sub>-686</sub>	93	103.795807	14.224410	2.0 ± 0.6	208 ± 9	915 <sup>+33</sup> <sub>-31</sub>
43	103.578790	13.925869	2.0 ± 0.4	205 ± 4	630 <sup>+247</sup> <sub>-140</sub>	94	103.795808	14.041406	3.7 ± 0.3	210 ± 2	2489 <sup>+316</sup> <sub>-255</sub>
44	103.579566	13.171484	1.0 ± 0.2	189 ± 5	428 <sup>+5</sup> <sub>-5</sub>	95	103.799506	14.333130	1.1 ± 0.2	172 ± 6	338 <sup>+4</sup> <sub>-4</sub>
45	103.610325	13.569492	1.4 ± 0.3	199 ± 4	2222 <sup>+145</sup> <sub>-129</sub>	96	103.804584	14.310143	2.4 ± 0.6	185 ± 7	1777 <sup>+195</sup> <sub>-161</sub>
46	103.613454	13.416918	1.7 ± 0.5	191 ± 7	6817 <sup>+1680</sup> <sub>-1261</sub>	97	103.804980	14.054295	3.3 ± 0.4	212 ± 3	3635 <sup>+603</sup> <sub>-463</sub>
47	103.615140	13.553508	2.2 ± 0.4	193 ± 4	347 <sup>+3</sup> <sub>-3</sub>	98	103.807211	14.052721	4.1 ± 0.1	211 ± 1	1267 <sup>+47</sup> <sub>-44</sub>
48	103.615277	13.441983	2.7 ± 0.8	207 ± 7	2376 <sup>+345</sup> <sub>-270</sub>	99	103.810584	14.308802	0.8 ± 0.3	210 ± 7	734 <sup>+19</sup> <sub>-18</sub>
49	103.620378	13.534314	2.5 ± 0.4	202 ± 4	889 <sup>+14</sup> <sub>-14</sub>	100	103.814455	13.573526	2.7 ± 0.9	190 ± 9	388 <sup>+8</sup> <sub>-8</sub>
50	103.622884	13.548024	2.1 ± 0.4	203 ± 5	1255 <sup>+37</sup> <sub>-35</sub>	101	103.817286	13.567570	4.1 ± 0.6	196 ± 4	4632 <sup>+896</sup> <sub>-672</sub>
51	103.625378	13.540711	2.5 ± 0.6	205 ± 6	700 <sup>+11</sup> <sub>-11</sub>	102	103.817426	14.327622	2.2 ± 0.6	213 ± 7	3948 <sup>+844</sup> <sub>-617</sub>

Table A.1. continued.

Star Id	$l$ (°)	$b$ (°)	$P \pm \sigma_P$ (%)	$\theta \pm \sigma_\theta$ (°)	$d \pm \sigma_d$ (pc)	Star Id	$l$ (°)	$b$ (°)	$P \pm \sigma_P$ (%)	$\theta \pm \sigma_\theta$ (°)	$d \pm \sigma_d$ (pc)
103	103.822409	14.433230	1.7 ± 0.4	183 ± 7	1160 <sup>+50</sup> <sub>-46</sub>	154	104.012635	14.040984	2.3 ± 0.5	203 ± 6	1071 <sup>+64</sup> <sub>-57</sub>
104	103.822561	14.466048	1.2 ± 0.3	170 ± 6	962 <sup>+19</sup> <sub>-18</sub>	155	104.013781	13.855258	1.9 ± 0.1	225 ± 2	2763 <sup>+173</sup> <sub>-154</sub>
105	103.824957	13.579997	2.9 ± 0.5	179 ± 5	1155 <sup>+76</sup> <sub>-68</sub>	156	104.017669	14.484564	1.4 ± 0.2	172 ± 4	572 <sup>+6</sup> <sub>-6</sub>
106	103.833996	14.484050	0.6 ± 0.1	174 ± 6	682 <sup>+11</sup> <sub>-10</sub>	157	104.022255	14.231824	1.9 ± 0.5	159 ± 7	1303 <sup>+104</sup> <sub>-90</sub>
107	103.834634	14.218497	2.0 ± 0.3	183 ± 5	918 <sup>+33</sup> <sub>-31</sub>	158	104.040345	14.029867	3.3 ± 0.2	210 ± 2	484 <sup>+5</sup> <sub>-5</sub>
108	103.837299	14.291510	1.7 ± 0.4	223 ± 7	2621 <sup>+352</sup> <sub>-280</sub>	159	104.040420	13.856945	2.7 ± 0.9	219 ± 9	1404 <sup>+40</sup> <sub>-38</sub>
109	103.841372	14.504933	1.6 ± 0.2	172 ± 3	4491 <sup>+643</sup> <sub>-510</sub>	160	104.041785	13.895636	4.7 ± 0.5	227 ± 3	441 <sup>+7</sup> <sub>-6</sub>
110	103.842941	14.199902	2.4 ± 0.6	188 ± 7	1252 <sup>+112</sup> <sub>-96</sub>	161	104.042081	13.844076	2.7 ± 0.8	230 ± 8	978 <sup>+23</sup> <sub>-22</sub>
111	103.848589	14.261173	4.0 ± 1.0	157 ± 7	973 <sup>+44</sup> <sub>-41</sub>	162	104.043729	14.115608	4.3 ± 0.3	204 ± 2	1105 <sup>+460</sup> <sub>-258</sub>
112	103.852653	14.485000	1.2 ± 0.2	165 ± 5	742 <sup>+51</sup> <sub>-45</sub>	163	104.049324	13.862234	2.3 ± 0.4	225 ± 5	734 <sup>+17</sup> <sub>-17</sub>
113	103.855020	13.592059	0.9 ± 0.1	182 ± 3	635 <sup>+1194</sup> <sub>-275</sub>	164	104.052854	13.842180	2.8 ± 0.2	223 ± 2	831 <sup>+30</sup> <sub>-28</sub>
114	103.858440	14.428986	1.3 ± 0.4	181 ± 8	990 <sup>+50</sup> <sub>-45</sub>	165	104.061791	14.012051	2.2 ± 0.2	199 ± 2	782 <sup>+12</sup> <sub>-12</sub>
115	103.867833	13.513033	0.9 ± 0.2	182 ± 4	1503 <sup>+30</sup> <sub>-29</sub>	166	104.061949	13.859067	4.2 ± 0.3	216 ± 2	4179 <sup>+451</sup> <sub>-374</sub>
116	103.872988	14.462072	0.8 ± 0.2	163 ± 8	1016 <sup>+27</sup> <sub>-26</sub>	167	104.068255	14.095157	2.3 ± 0.3	194 ± 4	2883 <sup>+363</sup> <sub>-293</sub>
117	103.873111	13.833073	2.0 ± 0.6	182 ± 8	1538 <sup>+124</sup> <sub>-107</sub>	168	104.077033	13.878035	2.1 ± 0.6	221 ± 8	654 <sup>+12</sup> <sub>-12</sub>
118	103.882462	13.779338	3.0 ± 0.5	192 ± 4	1312 <sup>+195</sup> <sub>-152</sub>	169	104.081708	13.949807	3.1 ± 0.5	209 ± 4	1483 <sup>+70</sup> <sub>-64</sub>
119	103.884349	14.449414	1.4 ± 0.3	160 ± 6	968 <sup>+33</sup> <sub>-31</sub>	170	104.085362	13.965820	3.0 ± 0.7	204 ± 6	1569 <sup>+59</sup> <sub>-55</sub>
120	103.884904	14.440311	1.7 ± 0.3	175 ± 4	1983 <sup>+147</sup> <sub>-128</sub>	171	104.095605	14.007224	4.0 ± 0.5	213 ± 3	936 <sup>+42</sup> <sub>-38</sub>
121	103.888410	14.261025	0.6 ± 0.1	203 ± 2	553 <sup>+6</sup> <sub>-6</sub>	172	104.097804	13.977882	2.8 ± 0.3	212 ± 3	4534 <sup>+659</sup> <sub>-521</sub>
122	103.889634	13.873195	3.7 ± 0.4	213 ± 3	2350 <sup>+227</sup> <sub>-191</sub>	173	104.100318	13.922871	2.1 ± 0.4	215 ± 5	1410 <sup>+39</sup> <sub>-37</sub>
123	103.890580	13.579406	1.7 ± 0.4	184 ± 6	1476 <sup>+30</sup> <sub>-29</sub>	174	104.102274	14.013854	3.5 ± 0.4	200 ± 3	1102 <sup>+39</sup> <sub>-36</sub>
124	103.894501	14.451970	1.5 ± 0.2	173 ± 4	445 <sup>+4</sup> <sub>-4</sub>	175	104.104955	13.879472	2.7 ± 0.9	225 ± 9	509 <sup>+10</sup> <sub>-10</sub>
125	103.895567	13.555001	0.7 ± 0.3	199 ± 8	761 <sup>+8</sup> <sub>-8</sub>	176	104.105705	13.906279	3.7 ± 0.4	228 ± 3	1721 <sup>+106</sup> <sub>-95</sub>
126	103.896591	14.258742	1.2 ± 0.3	207 ± 5	6048 <sup>+1554</sup> <sub>-1151</sub>	177	104.114463	13.968833	1.5 ± 0.5	222 ± 7	1341 <sup>+89</sup> <sub>-79</sub>
127	103.898571	13.623524	2.7 ± 0.7	201 ± 7	1569 <sup>+166</sup> <sub>-138</sub>	178	104.117886	13.985771	2.7 ± 0.4	211 ± 4	7276 <sup>+1546</sup> <sub>-1184</sub>
128	103.901924	14.271198	1.1 ± 0.2	200 ± 4	2243 <sup>+172</sup> <sub>-150</sub>	179	104.128116	14.231034	1.9 ± 0.4	157 ± 6	727 <sup>+28</sup> <sub>-26</sub>
129	103.907345	13.604975	2.5 ± 0.8	154 ± 8	518 <sup>+13</sup> <sub>-12</sub>	180	104.133295	13.852779	1.8 ± 0.3	60 ± 4	1025 <sup>+20</sup> <sub>-19</sub>
130	103.912882	13.847550	2.3 ± 0.2	225 ± 3	1370 <sup>+39</sup> <sub>-37</sub>	181	104.133852	14.389952	2.1 ± 0.3	177 ± 4	2857 <sup>+252</sup> <sub>-215</sub>
131	103.917862	13.901485	2.0 ± 0.1	211 ± 1	478 <sup>+5</sup> <sub>-5</sub>	182	104.141667	13.932187	3.3 ± 0.6	207 ± 5	1080 <sup>+29</sup> <sub>-27</sub>
132	103.920679	13.754134	1.9 ± 0.5	201 ± 5	8655 <sup>+1832</sup> <sub>-1428</sub>	183	104.146638	14.520769	1.1 ± 0.3	203 ± 8	3023 <sup>+341</sup> <sub>-281</sub>
133	103.924358	13.587156	1.8 ± 0.2	198 ± 4	800 <sup>+13</sup> <sub>-13</sub>	184	104.159392	14.566307	0.8 ± 0.1	165 ± 4	524 <sup>+4</sup> <sub>-4</sub>
134	103.925239	13.830119	1.5 ± 0.2	219 ± 3	522 <sup>+4</sup> <sub>-4</sub>	185	104.159795	13.895103	1.5 ± 0.3	205 ± 5	1230 <sup>+29</sup> <sub>-27</sub>
135	103.937410	14.509685	0.7 ± 0.2	159 ± 6	1066 <sup>+19</sup> <sub>-19</sub>	186	104.166900	14.377326	1.2 ± 0.4	171 ± 8	619 <sup>+16</sup> <sub>-15</sub>
136	103.941902	13.715247	1.2 ± 0.2	199 ± 3	1917 <sup>+50</sup> <sub>-48</sub>	187	104.174435	13.912937	1.4 ± 0.3	208 ± 6	6703 <sup>+1493</sup> <sub>-1126</sub>
137	103.942720	13.852638	2.5 ± 0.3	222 ± 3	2783 <sup>+155</sup> <sub>-140</sub>	188	104.177145	14.519745	2.1 ± 0.4	166 ± 5	8969 <sup>+1920</sup> <sub>-1521</sub>
138	103.943406	13.772898	2.1 ± 0.4	200 ± 5	1312 <sup>+39</sup> <sub>-37</sub>	189	104.180551	14.510612	0.8 ± 0.3	185 ± 8	1245 <sup>+29</sup> <sub>-27</sub>
139	103.946746	13.767981	1.2 ± 0.2	216 ± 3	849 <sup>+11</sup> <sub>-11</sub>	190	104.184877	14.463091	1.8 ± 0.2	179 ± 3	836 <sup>+14</sup> <sub>-14</sub>
140	103.949191	13.887192	2.1 ± 0.2	226 ± 3	3843 <sup>+501</sup> <sub>-403</sub>	191	104.189132	13.884124	2.4 ± 0.7	228 ± 8	1019 <sup>+63</sup> <sub>-56</sub>
141	103.955544	14.539678	1.5 ± 0.1	178 ± 3	3345 <sup>+235</sup> <sub>-207</sub>	192	104.190082	13.877895	1.6 ± 0.1	199 ± 1	2603 <sup>+156</sup> <sub>-140</sub>
142	103.970348	14.264221	4.6 ± 0.3	125 ± 2	2782 <sup>+870</sup> <sub>-571</sub>	193	104.190936	13.956342	1.4 ± 0.2	218 ± 4	1899 <sup>+62</sup> <sub>-59</sub>
143	103.970485	14.478970	1.0 ± 0.3	184 ± 7	2569 <sup>+213</sup> <sub>-184</sub>	194	104.196741	14.515530	1.5 ± 0.5	183 ± 7	3476 <sup>+561</sup> <sub>-433</sub>
144	103.976066	13.879128	3.2 ± 0.7	225 ± 6	3133 <sup>+435</sup> <sub>-345</sub>	195	104.201883	14.420479	2.0 ± 0.2	172 ± 3	2426 <sup>+169</sup> <sub>-149</sub>
145	103.983313	14.557376	1.1 ± 0.1	189 ± 3	2313 <sup>+100</sup> <sub>-92</sub>	196	104.203426	14.389243	0.8 ± 0.1	180 ± 4	318 <sup>+2</sup> <sub>-2</sub>
146	103.987328	14.504984	1.6 ± 0.1	183 ± 1	1593 <sup>+68</sup> <sub>-62</sub>	197	104.205921	13.888406	1.1 ± 0.3	202 ± 6	818 <sup>+10</sup> <sub>-9</sub>
147	103.994239	14.075042	1.5 ± 0.2	205 ± 3	1825 <sup>+1025</sup> <sub>-546</sub>	198	104.206816	14.410361	2.3 ± 0.7	166 ± 8	4192 <sup>+908</sup> <sub>-664</sub>
148	103.994364	13.897979	4.5 ± 1.0	228 ± 6	1769 <sup>+140</sup> <sub>-121</sub>	199	104.210431	14.400087	0.7 ± 0.2	186 ± 6	306 <sup>+2</sup> <sub>-2</sub>
149	103.996604	14.520752	1.9 ± 0.5	178 ± 7	584 <sup>+18</sup> <sub>-17</sub>	200	104.217190	14.287866	1.7 ± 0.5	52 ± 7	793 <sup>+11</sup> <sub>-11</sub>
150	104.004217	14.059293	3.9 ± 0.4	199 ± 3	1832 <sup>+168</sup> <sub>-143</sub>	201	104.222302	13.960593	1.2 ± 0.2	223 ± 3	957 <sup>+12</sup> <sub>-12</sub>
151	104.007753	13.895467	3.0 ± 0.6	228 ± 5	393 <sup>+4</sup> <sub>-4</sub>	202	104.229025	13.979337	1.0 ± 0.3	208 ± 7	473 <sup>+4</sup> <sub>-4</sub>
152	104.008566	14.116192	4.4 ± 0.2	193 ± 2	1413 <sup>+56</sup> <sub>-52</sub>	203	104.236310	13.952170	2.4 ± 0.7	217 ± 8	2034 <sup>+208</sup> <sub>-173</sub>
153	104.011561	13.846133	1.5 ± 0.3	221 ± 6	1639 <sup>+61</sup> <sub>-57</sub>	204	104.237648	14.540158	1.2 ± 0.2	163 ± 5	596 <sup>+7</sup> <sub>-7</sub>



Table A.1. continued.

Star Id	$l$ (°)	$b$ (°)	$P \pm \sigma_P$ (%)	$\theta \pm \sigma_\theta$ (°)	$d \pm \sigma_d$ (pc)	Star Id	$l$ (°)	$b$ (°)	$P \pm \sigma_P$ (%)	$\theta \pm \sigma_\theta$ (°)	$d \pm \sigma_d$ (pc)
205	104.242881	14.500877	$2.1 \pm 0.7$	$158 \pm 8$	$393^{+9}_{-8}$	228	104.356073	14.301893	$1.8 \pm 0.5$	$204 \pm 7$	$1307^{+55}_{-51}$
206	104.259147	14.495868	$1.3 \pm 0.3$	$168 \pm 6$	$1368^{+35}_{-33}$	229	104.358815	14.413296	$2.8 \pm 0.5$	$178 \pm 5$	$1058^{+44}_{-41}$
207	104.267690	13.917088	$1.1 \pm 0.2$	$196 \pm 6$	$1366^{+32}_{-31}$	230	104.359251	13.983480	$1.3 \pm 0.3$	$219 \pm 6$	$991^{+21}_{-20}$
208	104.270189	14.494670	$1.4 \pm 0.2$	$180 \pm 4$	$646^{+7}_{-7}$	231	104.362494	14.132594	$2.3 \pm 0.6$	$227 \pm 6$	$1516^{+121}_{-105}$
209	104.271671	14.537384	$1.3 \pm 0.2$	$166 \pm 3$	$1937^{+1333}_{-742}$	232	104.369866	14.251045	$3.8 \pm 0.4$	$197 \pm 3$	$2546^{+1433}_{-884}$
210	104.272463	14.479830	$2.4 \pm 0.6$	$182 \pm 7$	$462^{+9}_{-9}$	233	104.371279	14.155014	$3.4 \pm 0.5$	$198 \pm 4$	$949^{+171}_{-127}$
211	104.274425	13.991687	$2.3 \pm 0.5$	$215 \pm 6$	$2817^{+216}_{-188}$	234	104.371715	14.402114	$2.0 \pm 0.5$	$199 \pm 6$	$1246^{+32}_{-30}$
212	104.277089	14.354539	$5.3 \pm 0.6$	$185 \pm 3$	$2245^{+1431}_{-860}$	235	104.374637	14.199342	$1.6 \pm 0.2$	$220 \pm 4$	$1093^{+25}_{-24}$
213	104.277266	14.450763	$1.0 \pm 0.2$	$186 \pm 4$	$758^{+8}_{-8}$	236	104.374790	14.115005	$2.1 \pm 0.1$	$218 \pm 2$	$1744^{+102}_{-92}$
214	104.278619	14.449882	$1.1 \pm 0.1$	$185 \pm 2$	$3125^{+192}_{-172}$	237	104.375014	14.189853	$2.5 \pm 0.4$	$207 \pm 4$	$705^{+18}_{-17}$
215	104.325274	14.085256	$4.2 \pm 0.1$	$219 \pm 1$	$1902^{+214}_{-176}$	238	104.377829	14.145469	$3.9 \pm 0.4$	$218 \pm 3$	$1165^{+61}_{-56}$
216	104.325527	14.320067	$3.8 \pm 0.6$	$190 \pm 5$	$7381^{+1759}_{-1350}$	239	104.385528	14.097980	$1.1 \pm 0.3$	$222 \pm 8$	$2378^{+144}_{-129}$
217	104.326000	14.281308	$1.8 \pm 0.1$	$213 \pm 1$	$725^{+788}_{-263}$	240	104.390020	14.071041	$1.1 \pm 0.1$	$213 \pm 3$	$940^{+13}_{-12}$
218	104.327117	14.135960	$2.4 \pm 0.6$	$210 \pm 6$	$3112^{+287}_{-244}$	241	104.392257	14.247356	$2.6 \pm 0.4$	$200 \pm 4$	$3063^{+175}_{-158}$
219	104.332801	14.304419	$2.1 \pm 0.5$	$200 \pm 7$	$2125^{+143}_{-126}$	242	104.395140	14.329504	$3.4 \pm 0.6$	$187 \pm 4$	$1274^{+87}_{-77}$
220	104.334197	14.356322	$2.7 \pm 0.2$	$205 \pm 2$	$1205^{+27}_{-25}$	243	104.404037	14.248927	$3.0 \pm 0.3$	$205 \pm 3$	$2251^{+88}_{-82}$
221	104.337399	14.017642	$1.8 \pm 0.2$	$212 \pm 3$	$1622^{+35}_{-34}$	244	104.405975	14.334530	$2.7 \pm 0.6$	$206 \pm 6$	$1076^{+50}_{-46}$
222	104.342139	14.143725	$4.3 \pm 0.4$	$203 \pm 3$	$1341^{+87}_{-77}$	245	104.408042	14.326883	$2.1 \pm 0.6$	$190 \pm 7$	$1306^{+98}_{-86}$
223	104.347367	14.418693	$2.6 \pm 0.7$	$178 \pm 7$	$825^{+39}_{-35}$	246	104.414166	14.191229	$1.3 \pm 0.2$	$204 \pm 4$	$888^{+13}_{-12}$
224	104.348908	14.424935	$1.3 \pm 0.3$	$172 \pm 5$	$1049^{+25}_{-24}$	247	104.416347	14.309724	$2.5 \pm 0.8$	$203 \pm 8$	$1184^{+36}_{-34}$
225	104.350080	14.363166	$1.7 \pm 0.1$	$205 \pm 1$	$1778^{+86}_{-79}$	248	104.424996	14.165882	$2.0 \pm 0.4$	$188 \pm 6$	$2279^{+244}_{-202}$
226	104.351013	14.165030	$2.3 \pm 0.1$	$204 \pm 1$	$2633^{+98}_{-91}$	249	104.430929	14.299678	$3.5 \pm 0.7$	$206 \pm 6$	$2141^{+260}_{-211}$
227	104.355040	14.404310	$2.8 \pm 1.0$	$188 \pm 9$	$5245^{+922}_{-708}$						